

Biomolecular Simulations under Realistic Macroscopic Salt Conditions

Gregory A. Ross^{1,†}, Ariën S. Rustenburg^{1,2}, Patrick B. Grinaway^{1,2}, Josh Fass^{1,3}, John D. Chodera^{1*}

¹Computational and Systems Biology Program, Sloan Kettering Institute, Memorial Sloan Kettering Cancer Center, New York, NY 10065; ²Graduate Program in Physiology, Biophysics, and Systems Biology, Weill Cornell Medical College, New York, NY 10065; ³Tri-Institutional Training Program in Computational Biology and Medicine, New York, NY 10065

Abstract Biomolecular simulations are typically performed in an aqueous environment where the number of ions remains fixed for the duration of the simulation, generally with either a minimally neutralizing ion environment or a number of salt pairs intended to match the macroscopic salt concentration. In contrast, real biomolecules experience local ion environments where the salt concentration is dynamic and may differ from bulk. The degree of salt concentration variability and average deviation from the macroscopic concentration remains, as yet, unknown. Here, we describe the theory and implementation of a Monte Carlo *osmostat* that can be added to explicit solvent molecular dynamics or Monte Carlo simulations to sample from a semigrand canonical ensemble in which the number of salt pairs fluctuates dynamically during the simulation. The osmostat reproduce the correct equilibrium statistics for a simulation volume that can exchange ions with a large reservoir at a defined macroscopic salt concentration. To achieve useful Monte Carlo acceptance rates, the method makes use of nonequilibrium candidate Monte Carlo (NCCMC) moves in which monovalent ions and water molecules are alchemically transmuted using short nonequilibrium trajectories, with a modified Metropolis-Hastings criterion ensuring correct equilibrium statistics for an $(\Delta\mu, N, p, T)$ ensemble. We demonstrate how typical protein (DHFR and the tyrosine kinase Src) and nucleic acid (Drew-Dickerson B-DNA dodecamer) systems exhibit salt concentration distributions that significantly differ from fixed-salt bulk simulations and display fluctuations that are on the same order of magnitude as the average.

***For correspondence:**

john.chodera@choderalab.org (John D. Chodera)

Present address: [†]Schrödinger, New York, NY 10036

1

2 Introduction

3 Molecular dynamics simulations have proven themselves a powerful tool for studying the structure, dynamics,
4 and function of biomolecular systems in atomic detail. Current state-of-the-art approaches simulate a small
5 volume around the biomolecule using explicit atomistic solvent to model the local environment. To more
6 realistically emulate electrostatic screening effects in the local solvent environment, explicit ions are generally
7 added, both to achieve net neutrality and to mimic the macroscopic salt concentration in the *in vitro* or *in*

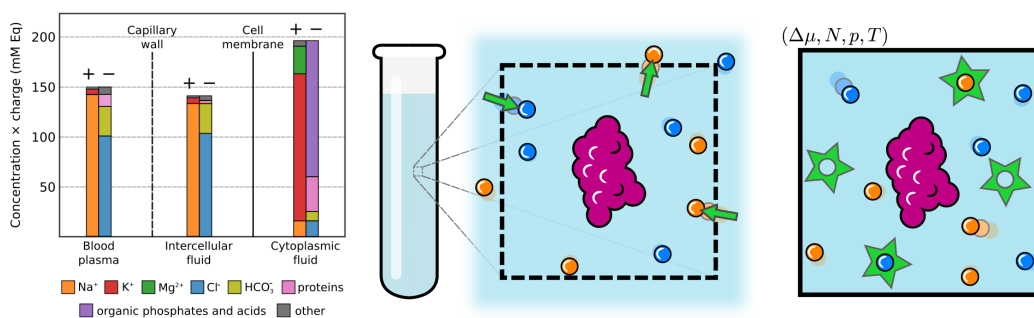


Figure 1. Schematic illustrations of typical salt concentrations in mammalian environments and anions and cations being exchanged with a saline buffer in the region around a biomolecule.

Left: The ion compositions of intra- and intercellular mammalian environments are shown as *millimolar equivalents* (mM Eq), which is the ion concentration multiplied by the absolute charge of the ion. The primary contribution to the ionic-strength are monovalent ions (Na⁺, K⁺, Cl⁻), divalent cations (predominantly Mg²⁺), complex salt and buffer molecules, and charged proteins. In addition to the significant difference between the ionic composition of the cytoplasmic fluid and extracellular fluid, organelles can also have markedly different ionic concentrations to the cytoplasmic fluid¹. Over large lengthscales, environments are approximately electrostatically neutral; electrostatic potentials across cell membranes are maintained by an imbalance of anions and cations that is minuscule relative to the total number ions². Figure adapted from² and³. *Middle:* In a very large system, where the number of water molecules and number of ions are fixed, significant fluctuations can occur in the ionic strength of the local environment of a biomolecule (in purple). The local environment is represented by a dashed line, within which the number of water molecules and ions fluctuate at equilibrium. *Right:* A simulation with an osmostat replicates the natural variations in ionic strength around a biomolecule that would occur if the system were embedded in an infinite saline reservoir at a fixed macroscopic salt concentration. Anions and cations (blue and orange spheres) are inserted and deleted (green stars) from the system using semigrand canonical Monte Carlo moves that exchange explicit water molecules for the ions in a manner that maintains total charge neutrality. The reservoir is completely defined by its thermodynamic parameters, which in this case include the difference in the chemical potential for two water molecules and NaCl, $\Delta\mu$ ($= \Delta\mu_{2\text{-H}_2\text{O}-\text{NaCl}}$), pressure p , and temperature, T .

8 *in vivo* environment being studied.

9 Salt concentrations and ionic composition are tightly regulated in biology⁴. Ion composition differs
 10 between inter/intracellular environments², tumor microenvironments⁵, and organelles¹ (see Figure 1,
 11 *left*). The local ionic concentration in the environment around real biological macromolecules, however,
 12 can significantly deviate from macroscopic concentrations. Many biomolecules possess a significant net
 13 charge, and the energetic penalty for physical systems to maintain charge separation over large distances
 14 serves to recruit more or less ions from bulk to maintain charge neutrality over macroscopic lengthscales.
 15 Yet, the number of ions within the immediate vicinity may not necessarily counter the net charge of the
 16 macromolecule, as proteins can predominantly bind to ions that have the same polarity as their net charge⁶.
 17 Additionally, statistical fluctuations in the total number of ions in the region around the biomolecule may
 18 result in significant variance in the local salt concentration, where relative concentration fluctuations diminish
 19 slowly with increasing simulation volume (Figure 1, *middle*).

20 Biomolecular behavior can be sensitive to salt environments

21 The conformations, dynamics, function, and binding of biological macromolecules can be exquisitely sensitive
 22 to the salt concentration and composition of the local environment. The Hofmeister effect, in which ions
 23 modulate the strength of the hydrophobic effect—a major driving force in protein folding and association^{7,8}—
 24 has been known since at least the nineteenth century⁹⁻¹¹. Biomolecular interactions involving highly charged
 25 nucleic acids—such as DNA:protein interactions critical for DNA repair¹²—have been observed to show
 26 sensitivity to macroscopic salt concentrations¹³, as have DNA:antibiotic interactions¹⁴. In the realm of
 27 pharmaceutical design, where there is great interest in engineering small molecule ligands, salt effects are
 28 known to modulate the interactions of small molecules with proteins¹⁵ or with supramolecular hosts¹⁶.

29 Current simulation practice arbitrarily fixes microscopic salt composition

30 In contrast to real physical systems, where the local region near the biomolecule is able to exchange ions with
31 a macroscopic reservoir at a fixed salt concentration (Figure 1, *middle*), simulations of biomolecules typically
32 fix the *number* of salt molecules present in the simulation volume. There is a great deal of diversity in how the
33 fixed number of added ions is typically determined: Along with the specified macroscopic ion concentration,
34 simulation packages may make use of the total cell volume (e.g., Gromacs¹⁷), the total solvent volume
35 excluding the biomolecular solutes (e.g., CHARMM-GUI¹⁸), or the number of water molecules (converting the
36 ion concentration into mole or mass fraction, as in OpenMM^{19,20}). Some simulation packages choose to use
37 only minimal neutralizing counterions or no counterions at all, relying on uniform background neutralizing
38 charge to allow treatment of long-range electrostatics by particle mesh Ewald (PME) methods^{21,22} (such as
39 Schrödinger's FEP+ alchemical free energy calculations²³). In simulation volumes large enough to mimic the
40 inclusion of a macroscopic salt reservoir far from the biomolecular system of interest, the environment near
41 the biomolecule may be accurately represented, but long correlation times for well-ordered ions may still
42 hinder equilibration of the ion environment^{24–26}.

43 Simulations in the semigrand canonical ensemble can mimic real salt fluctuations

44 Simulations in the (semi)grand canonical ensemble, however, can—at least in principle—remedy this situation
45 by explicitly allowing one or more components (such as ions) to fluctuate over the course of the simulation
46 via *grand canonical Monte Carlo* (GCMC) moves (Figure 1, *right*). In grand and semigrand canonical methods,
47 simulations are placed in thermodynamic equilibrium with a theoretical reservoir of components. The
48 simulation can exchange molecules/particles with the reservoir, and the concentration the components in
49 the reservoir are specified by their respective chemical potentials. Before running these simulations, one
50 first has to determine the mapping between the concentration in the reservoir and chemical potentials, a
51 process we refer to as *calibration*. Sampling over ion concentrations in explicit water via straightforward
52 GCMC is difficult: Monte Carlo insertion/deletions have to overcome long-range effects, low acceptance rates
53 for instantaneous Monte Carlo moves, and the concentration is sensitive to small ($< k_B T$) variations in the
54 chemical potential. Some efforts have circumvented these issues by using implicit solvent models^{6,27}, cavity-
55 biased insertions in specialized solvent models²⁸, and explicit solvent reorganization moves²⁹. *Osmotic*
56 *ensemble Monte Carlo* schemes that use fractional ions and Wang-Landau approaches have also proven
57 themselves to be useful in simulations of simple aqueous electrolytes^{30,31}.

58 Nonequilibrium candidate Monte Carlo (NMC) can achieve high acceptance rates

59 More recently, nonequilibrium candidate Monte Carlo (NMC) has been shown to be an effective solution to
60 the problem of low acceptance rates when inserting or deleting particles³². In contrast to an instantaneous
61 Monte Carlo (MC) proposal in which an inserted particle is switched instantaneously on and may clash with
62 other solvent or solute particles, in an NMC proposal, the particle is switched on slowly as the system is
63 allowed to relax via some form of dynamics. NMC uses a modified acceptance criteria that incorporates
64 the nonequilibrium work to ensure that the resulting endpoints sample from the equilibrium distribution.
65 With well-tuned nonequilibrium protocols, NMC acceptance rates can be astronomically higher than their
66 instantaneous MC counterparts³². In work simulating biomolecules at constant-pH, for example, Roux and
67 coworkers have demonstrated how NMC is effective at achieving high acceptance rates for NMC proposals
68 that also transmute an ion to/from a water molecule to maintain net charge neutrality of the system^{33,34}.

69 While calibration of the effective chemical potential for the water and ion forcefields and simulation
70 parameters at hand is nontrivial, this technical challenge can be satisfyingly addressed with existing technol-
71 ogies: Self-adjusted mixture sampling (SAMS)³⁵, a form of adaptive expanded ensemble sampling³⁶, can be
72 used to conveniently achieve uniform sampling of all relevant salt concentrations in a single simulation, while
73 the Bennett acceptance ratio (BAR) can optimally extract estimates of the relevant free energy differences
74 from all NMC proposals along with good estimates of statistical error and minimal bias^{37–39}. Independent
75 simulations at each salt concentration could be performed separately, with nonequilibrium switching trajec-
76 tories used to estimate relative free energies between different numbers of salt pairs. However, SAMS helps
77 more rapidly decorrelate the configurations of ions and, in principle, allows a single simulation to be used

78 for calibration.

79 An NCMC osmostat can be used alongside thermostats and barostats

80 Here, we present a new approach that makes use of NCMC to insert/delete salt pairs with high acceptance
81 probability in a manner that correctly models the statistical mechanics of exchange with a macroscopic salt
82 reservoir. The osmostat needs to be calibrated once for the specified solvent and ion models, simulation
83 parameters, and thermodynamic conditions (temperature, pressure, pH, etc.). Following calibration, the
84 osmostat is used in a manner similar to a Monte Carlo barostat, attempting to modify the system composition
85 (and hence interaction potential) at regular intervals to ensure sampling from a target probability density
86 that models a system in equilibrium with a macroscopic salt reservoir (Figure 2). Similar to a Monte Carlo
87 barostat^{19,40}, the osmostat moves can be integrated alongside molecular dynamics simulations and other
88 Monte Carlo schemes to sample from equilibrium distributions with specified thermodynamic control
89 parameters. This composability is a general feature of Markov chain Monte Carlo moves, which provide a
90 useful framework for designing modular algorithms for biomolecular simulation⁴¹.

91 How do salt environments vary in realistic biomolecular simulations?

92 Once we have developed and validated this tool, we use it to ask biophysical questions about the nature of salt
93 environments around biological macromolecules: What is the average salt concentration in the simulation
94 volume, and how does it compare to bulk? Which heuristic scheme, if any, most closely approximates the
95 local salt concentration: macroscopic concentration times total cell volume or solvent volume, or mole
96 fraction of water molecules? How much does the local salt concentration and ionic strength vary in “typical”
97 biomolecular simulation conditions for different classes of biomolecular systems, such as proteins and
98 nucleic acids? And can a Monte Carlo osmostat reduce correlation times for ions over that seen in standard
99 MD simulations, such as the slow correlation times in ion environments around nucleic acids²⁵? We consider
100 some test systems that represent different classes of common biomolecular simulations: TIP3P⁴² (and
101 TIP4P-Ew⁴³) water boxes, dihydrofolate reductase (DHFR), the *apo* kinase Src, and the Drew-Dickerson B-DNA
102 dodecamer²⁵ as a typical nucleic acid.

103 Outline

104 This paper is organized as follows: First, we review the theory behind (semi)grand canonical ensembles that
105 model the fluctuations experienced by small subvolumes surrounding biomolecules. Second, we describe
106 the algorithmic design of the osmostat used to allow salt concentrations to fluctuate dynamically. Finally, we
107 apply the osmostat to address biophysical questions of interest and discuss the nature of salt distributions
108 and their fluctuations.

109 Theory and methodology

110 An NCMC osmostat for sampling ion fluctuations in the semigrand ensemble

111 An *osmostat* is like a thermostat or barostat but allows the number of salt pairs in the simulation box
112 to change dynamically under the control of a conjugate thermodynamic parameter—here, the chemical
113 potential of salt. Salt pairs can be thought of as being exchanged with a macroscopic reservoir, with the
114 free energy to add or remove salt to this reservoir described by the applied chemical potential. In principle,
115 an osmostat could be implemented by including a number of noninteracting (“ghost”) molecules in the
116 simulation volume, turning their interactions on and off to allow the number of active salt molecules to
117 fluctuate dynamically; alternatively, new salt molecules could be introduced or removed dynamically using
118 reversible-jump Monte Carlo (RJMC) methods⁴⁴. In either case, solvent cavity formation to accommodate
119 ions would almost certainly require nonequilibrium protocols that employ soft-core potentials and significant
120 tuning of these insertion/deletion protocols to achieve high acceptance rates.

121 To simplify implementation for the ions most commonly used in biomolecular simulations (such as NaCl
122 or KCl), we instead choose to exchange the *identities* of water molecules and salt ions, where our conjugate
123 thermodynamic parameter $\Delta\mu_{2\text{H}_2\text{O}-\text{NaCl}}$ (which we will abbreviate as $\Delta\mu$) will represent the difference in
124 chemical potential between withdrawing an NaCl molecule from the reservoir while returning two H₂O

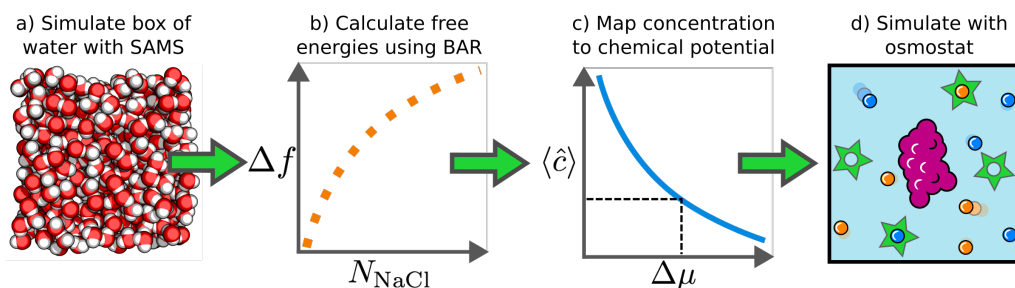


Figure 2. Schematic illustration of the workflow used to calibrate and implement the osmostat. (a) Self-adjusted mixture sampling (SAMS) simulations sample an entire range of salt pairs, $N_{\text{NaCl}} \in [0, N_{\text{NaCl, max}}]$, in a sufficiently large box of water to model a saline reservoir. Nonequilibrium candidate Monte Carlo (NEMC) is used to achieve high acceptance rates during salt insertion/deletion attempts, in which an NaCl molecule is transformed into a pair of water molecules, or vice versa. (b) The Bennett acceptance ratio (BAR) estimator uses the work values from *all* NEMC proposals (including rejected proposals) to compute an optimal estimate of the (dimensionless) relative free energy, $\Delta f(N_{\text{NaCl}}) \equiv f(N_{\text{NaCl}} + 1) - f(N_{\text{NaCl}})$, to add an additional NaCl salt pair to the box of saline as a function of the number of salt pairs already present, N_{NaCl} . BAR allows $f(N_{\text{NaCl}})$ to be estimated to a higher precision than the estimates from SAMS. (c) Once $\Delta f(N_{\text{NaCl}})$ has been computed for the desired water/ion forcefield and simulation parameters governing the energy computation (such as long-range electrostatics treatment), the chemical potential $\Delta\mu$ that produces the desired macroscopic salt concentration $\langle \hat{c} \rangle$ is numerically computed using equation 19. (d) This same chemical potential $\Delta\mu$ is subsequently used as the thermodynamic parameter governing the osmostat to simulate a biomolecular system in equilibrium with an infinitely sized saline reservoir at the specified macroscopic salt concentration.

125 molecules. Because solvent cavities are not being created or destroyed—only modified slightly in size—this
 126 should provide superior phase space overlap between initial and final states.

127 We denote the total number of water molecules and ions as N , and define the identities of the water
 128 molecules and ions with the vector $\theta = (\theta_1, \theta_2, \dots, \theta_N)$ with $\theta_i \in \{-1, 0, +1\}$ to denote anions ($\theta_i = -1$), water
 129 ($\theta_i = 0$), and cations ($\theta_i = +1$), respectively (with the potential to extend this to divalent ions by adding $-2, +2$).
 130 This choice of labeling allows us to define the total number of Na^+ ions as

$$N_{\text{Na}^+}(\theta) = \sum_i^N \delta(+1, \theta_i), \quad (1)$$

131 the total number of Cl^- ions as

$$N_{\text{Cl}^-}(\theta) = \sum_i^N \delta(-1, \theta_i), \quad (2)$$

132 and the number of water molecules as

$$N_{\text{H}_2\text{O}}(\theta) = \sum_i^N \delta(0, \theta_i), \quad (3)$$

133 where $\delta(x, y)$ denotes the Kronecker delta, which is unity when $x = y$ and zero otherwise, and sums run from
 134 i to N . Note that the total number of waters and ions, $N \equiv N_{\text{Na}^+}(\theta) + N_{\text{Cl}^-}(\theta) + N_{\text{H}_2\text{O}}(\theta)$, is fixed, and does not
 135 depend on θ . We define the total charge number of the biomolecules, excluding counterions, as z .

136 When $z \neq 0$, counterions will be added to ensure that the total charge of the simulation system is zero.
 137 The system can be neutralized by any of choice of θ that satisfies $n(\theta) = -z$, where the total charge due to
 138 ions is given by

$$n(\theta) = \sum_i^N \theta_i. \quad (4)$$

139 As neutralizing the system will lead to unequal numbers of Na^+ and Cl^- , we define the amount of salt as the
 140 number of neutral pairs,

$$N_{\text{NaCl}}(\theta) \equiv \min\{N_{\text{Na}^+}(\theta), N_{\text{Cl}^-}(\theta)\}. \quad (5)$$

141 The semigrand ensemble models salt exchange with a macroscopic salt reservoir
 142 When our osmostat is combined with a scheme that samples the isothermal-isobaric (N, p, T) ensemble,
 143 we formally sample the semigrand-isothermal-isobaric ensemble $(\Delta\mu, N, p, T)$. The associated equilibrium
 144 probability density is given by

$$\pi(x, \theta; \Delta\mu, N, p, T) = \frac{1}{\Xi(\Delta\mu, N, p, T)} \delta(n(\theta), -z) e^{-\beta[U(x, \theta) + pV(x) + \Delta\mu N_{\text{NaCl}}(\theta)]}, \quad (6)$$

145 where the Kronecker delta $\delta(n(\theta), -z)$ imposes net charge neutrality, $\beta \equiv 1/k_B T$ is the inverse temperature,
 146 and $\Xi(\Delta\mu, N, p, T)$ is the normalizing constant, given by

$$\Xi(\Delta\mu, N, p, T) = \sum_{\theta} \delta(n(\theta), -z) \int dx e^{-\beta[U(x, \theta) + pV(x) + \Delta\mu N_{\text{NaCl}}(\theta)]}, \quad (7)$$

147 where the outer sum is over all identity vectors and the integral is over all configuration space. For brevity,
 148 the dependence of π and Ξ on z will be omitted. It is also possible to express the probability density of
 149 the system as a function of the total number of cations and anions, rather than as function of θ . This can
 150 be achieved by summing $\pi(x, \theta; \Delta\mu, N, p, T)$ over all identity vectors that preserve the neutral charge of the
 151 system and $N_{\text{NaCl}}(\theta)$ at some constant value N'_{NaCl} :

$$\begin{aligned} \pi(x, N'_{\text{NaCl}}; \Delta\mu, N, p, T) &= \sum_{\theta} \delta(N_{\text{NaCl}}(\theta), N'_{\text{NaCl}}) \pi(x, \theta; \Delta\mu, N, p, T) \\ &\propto \frac{N!}{N'_{\text{Na}^+}! N'_{\text{Cl}^-}! N'_{\text{H}_2\text{O}}!} e^{-\beta[U(x; N'_{\text{NaCl}}) + pV(x) + \Delta\mu N'_{\text{NaCl}}]}, \end{aligned} \quad (8)$$

152 where $U(x; N'_{\text{NaCl}})$ is the potential energy for a system with fixed particle identities that contains N'_{NaCl} salt
 153 pairs. The factorial prefactors account for the degeneracy number of identity vectors θ that satisfy the
 154 constraints $N_{\text{NaCl}}(\theta) = N'_{\text{NaCl}}$ and $n(\theta) + z = 0$.

155 Gibbs sampling provides a modular way to sample from the semigrand ensemble
 156 A Gibbs sampling framework can be used to create a modular simulation scheme in which the osmostat
 157 updates molecular identities infrequently while some MCMC scheme (such as Metropolis Monte Carlo or
 158 Metropolized molecular dynamics) updates particle positions using fixed particle identities:

$$x \sim \pi(x|\theta, N, p, T) \propto e^{-\beta[U(x, \theta) + pV(x)]} \quad (9)$$

$$\theta \sim \pi(\theta|x, \Delta\mu, N, p, T) \propto e^{-\beta[U(x, \theta) + \Delta\mu N_{\text{NaCl}}(\theta)]} \quad (10)$$

159 By embedding this approach in a Gibbs sampling framework, it allows the osmostat to readily be combined
 160 with other sampling schemes that make use of a Gibbs sampling framework such as replica exchange and
 161 expanded ensemble simulations⁴⁵.

162 Instead of instantaneous MC switching to propose changes in the chemical identities θ at fixed configura-
 163 tion x , nonequilibrium candidate Monte Carlo (NCMC) is used to propose updates of chemical identities and
 164 positions simultaneously as sufficiently long switching trajectories can sampling efficiencies that are orders
 165 of magnitude larger than instantaneous proposals³²:

$$x \sim \pi(x|\theta, N, p, T) \propto e^{-\beta[U(x, \theta) + pV(x)]} \quad (11)$$

$$x, \theta \sim \pi(x, \theta|N, p, T, \Delta\mu) \propto e^{-\beta[U(x, \theta) + pV(x) + \Delta\mu N_{\text{NaCl}}(\theta)]} \quad (12)$$

166 NCMC uses a modified Metropolis-Hastings acceptance protocol in which the appropriate *total work* for
 167 switching is accumulated during the nonequilibrium proposal and used in the acceptance criterion.

168 The chemical potential $\Delta\mu$ must be calibrated to model macroscopic salt concentrations
 169 Simulating a system that is in chemical equilibrium with an infinitely large saline reservoir at a specified
 170 salt concentration first requires the calibration of the chemical potential $\Delta\mu$. There are multiple ways that
 171 one could compute the necessary chemical potential. For instance, one could approximate the reservoir
 172 with a sufficiently large box of water, and narrow-in on the chemical potential that produces the desired
 173 salt concentration using stochastic approximation or the density control method recommended by Spedal

174 et al.⁴⁶. However, this requires carrying out separate calibration calculations for each desired macroscopic
 175 concentration. Instead, we aim to construct a simple calibration procedure by computing the free energies to
 176 insert salt pairs into a sufficiently large box of water. We then use these free energies to analytically compute
 177 macroscopic salt concentrations over a wide range of chemical potentials, providing a relationship that can
 178 be numerically inverted. This procedure need be done only once for a specified ion and water model, though
 179 it may need to be repeated if the method used to compute long-range electrostatic interactions is modified.

180 Our calibration method is similar in principle to that of Benavides et al.⁴⁷, who estimated the chemical
 181 potential of NaCl by calculating the free energy to insert NaCl to over a range of concentrations. However,
 182 unlike⁴⁷—where the goal was to estimate the solubility of NaCl—our interest in estimating the chemical
 183 potential lies solely in its ability to determine the chemical potential of the osmostat saline reservoir corre-
 184 sponding to the desired macroscopic salt concentration in order to induce the appropriate salt distribution
 185 on microscopic simulation systems.

186 Our approach to calibration computes the free energies to add $N_{\text{NaCl}} \in \{1, 2, \dots, N_{\text{NaCl, max}}\}$ salt pairs to
 187 an initially pure box of water. We limit our free energies calculations to insert NaCl up to some maximum
 188 $N_{\text{NaCl, max}} \ll N$ for practical convenience. No constraint is placed on the amount of salt that can be added in
 189 osmostat simulations—instead, the value of $N_{\text{NaCl, max}}$ impacts the accuracy with which the osmostat can
 190 reproduce high macroscopic salt concentrations. We define the absolute dimensionless free energy of a
 191 system with N_{NaCl} salt pairs at pressure p and temperature T as $f(N_{\text{NaCl}}, N, p, T)$,

$$f(N_{\text{NaCl}}, N, p, T) \equiv -\ln \left(\frac{Z(N_{\text{NaCl}}, N, p, T)}{Z(0, N, p, T)} \right), \quad (13)$$

192 where the partition function $Z(N'_{\text{NaCl}}, N, p, T)$ is given by

$$Z(N'_{\text{NaCl}}, N, p, T) = \sum_{\theta} \delta(N_{\text{NaCl}}(\theta), N'_{\text{NaCl}}) \int dx e^{-\beta[U(x, \theta) + pV(x)]} \quad (14)$$

$$= \frac{N!}{N'_{\text{Na}^+}! N'_{\text{Cl}^-}! N'_{\text{H}_2\text{O}}!} \int dx e^{-\beta[U(x; N'_{\text{NaCl}}) + pV(x)]}, \quad (15)$$

193 where the number of water molecules $N'_{\text{H}_2\text{O}} = N' - 2 \cdot N'_{\text{NaCl}}$. For convenience, we define relative free energies
 194 as

$$\Delta f(N_{\text{NaCl}}, N, p, T) \equiv f(N_{\text{NaCl}} + 1, N, p, T) - f(N_{\text{NaCl}}, N, p, T). \quad (16)$$

195 For simplicity, we shall use $f(N_{\text{NaCl}})$ and $\Delta f(N_{\text{NaCl}})$ as abbreviations to equations 13 and 16, respectively. The
 196 free energies $f(N_{\text{NaCl}})$ can then be used to calculate the average number of salt pairs as a function of the
 197 chemical potential $\Delta\mu$,

$$\langle N_{\text{NaCl}} \rangle_{\Delta\mu, N, p, T} = \Xi(\Delta\mu, N, p, T)^{-1} \sum_{N_{\text{NaCl}}=0}^{N_{\text{NaCl, max}}} N_{\text{NaCl}} e^{-f(N_{\text{NaCl}}) + \beta\Delta\mu N_{\text{NaCl}}} \quad (17)$$

198 where the semigrand partition function $\Xi(\Delta\mu, N, p, T)$ (the same one from equation 7) can be compactly
 199 written as

$$\Xi(\Delta\mu, N, p, T) = \sum_{N_{\text{NaCl}}=0}^{N_{\text{NaCl, max}}} e^{-f(N_{\text{NaCl}}) + \beta\Delta\mu N_{\text{NaCl}}} \quad (18)$$

200 Knowledge of $f(N_{\text{NaCl}})$ will also provide a convenient estimate of the macroscopic salt concentration. We
 201 define the macroscopic salt concentration as the mean salt concentration of a system in the thermodynamic
 202 limit, and derive in Appendix 2 the following expression for the macroscopic concentration that is amenable
 203 to computational analysis:

$$\langle \hat{c} \rangle_{\Delta\mu, N, p, T} = \frac{\sum_{N_{\text{NaCl}}=0}^{N_{\text{NaCl, max}}} N_{\text{NaCl}} e^{-f(N_{\text{NaCl}}) + \beta\Delta\mu N_{\text{NaCl}}}}{\sum_{N_{\text{NaCl}}=0}^{N_{\text{NaCl, max}}} \langle V \rangle_{N_{\text{NaCl}}, N, p, T} e^{-f(N_{\text{NaCl}}) + \beta\Delta\mu N_{\text{NaCl}}}}, \quad (19)$$

204 where $\langle V \rangle_{N_{\text{NaCl}}, N, p, T}$ is the average volume for a fixed N_{NaCl} . The macroscopic concentration $\langle \hat{c} \rangle_{\Delta\mu, N, p, T}$ is a
205 monotonic function of the chemical potential $\Delta\mu$. Therefore—provided one has estimates of $f(N_{\text{NaCl}})$ and
206 $\langle V \rangle_{N_{\text{NaCl}}, N, p, T}$ —the value of the chemical potential $\Delta\mu(c)$ that yields a desired macroscopic concentration
207 $\langle \hat{c} \rangle_{\Delta\mu, N, p, T}$ can be obtained by numerically inverting equation 19.

208 Free energies for salt insertion can be efficiently computed using SAMS

209 One could estimate the free energies $f(N_{\text{NaCl}})$ $N_{\text{NaCl}} \in \{0, 1, \dots, N_{\text{NaCl}, \text{max}}\}$ using a $N_{\text{NaCl}, \text{max}} - 1$ equilibrium
210 calculations of the relative free energies $\Delta f(N_{\text{NaCl}})$ or the recently developed grand canonical integration
211 technique^{48,49}. As the latter requires *a priori* knowledge of the approximate scaling of the chemical potential
212 with the concentration, we instead opt to use the recently proposed self-adjusted mixture sampling (SAMS)³⁵
213 method to facilitate the calculation of the free energies from a single simulation. SAMS is a development
214 on the method of expanded ensembles³⁶ (sometimes known as serial tempering⁵⁰) and generalized Wang-
215 Landau algorithms^{51,52}. It is a stochastic approximation scheme that produces unbiased estimates of the
216 free energies (unlike Wang-Landau) that—in the asymptotic limit—have the lowest variance out of all other
217 stochastic approximation recursion schemes³⁵. It can be used to sample over a discrete state space and
218 simultaneously estimate the relative log-normalizing constant for each state. For our calibration simulations,
219 the discrete states correspond to the number of salt pairs in the systems $N_{\text{NaCl}} \in \{0, 1, \dots, N_{\text{NaCl}, \text{max}}\}$ and the
220 log-normalizing constant are the desired free energies $f(N_{\text{NaCl}})$. By dynamically altering a series of biasing
221 potentials, one for each state, the SAMS algorithm asymptotically samples the discrete states according to
222 user specified target weights³⁵. When the target weights are uniform over the state space—as we choose
223 herein to ensure the uncertainties in the estimated free energies are approximately equal—the biasing
224 potentials are themselves estimates of the free energies $f(N_{\text{NaCl}})$. Thus, SAMS can, in principle, calculate all
225 $f(N_{\text{NaCl}})$ in a single simulation more efficiently and conveniently than numerous independent equilibrium
226 free energy calculations.

227 As we describe below, our osmostat employs NCMC, which allows us to calculate the salt-insertion free
228 energies by processing all of the NCMC protocol work values in the SAMS simulations with BAR, even from
229 the attempts that are rejected. BAR requires samples of forward and reverse work samples of salt insertion
230 and deletion attempts to compute $\Delta f(N_{\text{NaCl}})$ and its statistical uncertainty for $N_{\text{NaCl}} \in \{0, 1, \dots, N_{\text{NaCl}, \text{max}}\}$ ³⁷⁻³⁹.
231 These relative free energies can then be summed to estimate $f(N_{\text{NaCl}})$ and corresponding statistical uncer-
232 tainties. Our calibration simulations therefore exploit the sampling efficiency of SAMS and the estimation
233 efficiency of BAR.

234 In general, the chemical potential $\Delta\mu$ will need to be recalibrated if the practitioner changes temperature,
235 pressure, water or ion forcefield models, nonbonded treatment, or anything that will affect $f(N_{\text{NaCl}})$ or
236 $\langle V \rangle_{N_{\text{NaCl}}, N, p, T}$. A sufficiently large water box must be used when calculating $f(N_{\text{NaCl}})$ to reach a regime in which
237 $f(N_{\text{NaCl}})$ is insensitive to changes in simulation size; as we will show, our calibration simulations achieve this
238 size insensitivity even for modest water boxes of a few thousand molecules.

239 The osmostat maintains electrostatic neutrality

240 To use PME²¹, a popular choice for accurate long-range electrostatics, charge neutrality of the entire
241 system needs to be maintained to avoid the artifacts induced by application of a uniform background
242 neutralizing charge²². Even if an alternative long-range electrostatics treatment is employed (e.g. reaction
243 field electrostatics or other non-Ewald methods⁵³), there is, in general, approximate equality between the
244 total number of negative charges and positive charges in biological microenvironments as they approach
245 macroscopic lengthscales (see Figure 1 *left*). From a purely theoretical perspective, the existence of a
246 thermodynamic limit a system with a net charge depends on the particular details of the system⁵⁴. For these
247 reasons, we ensure that our proposals always maintain charge neutrality by inserting or deleting a neutral
248 Na^+ and Cl^- pair.

249 We insert and delete a salt pair by converting Na^+ and Cl^- ions to two water molecules (see Figure 3).
250 These moves convert the nonbonded forcefield parameters (partial charges q , Lennard-Jones radii σ , and
251 Lennard-Jones potential well-depths ϵ) of the water and ion parameters. The Na^+ and Cl^- ions are given the
252 same topology, geometry, and number of atoms as the water model used for the simulation. Irrespective of

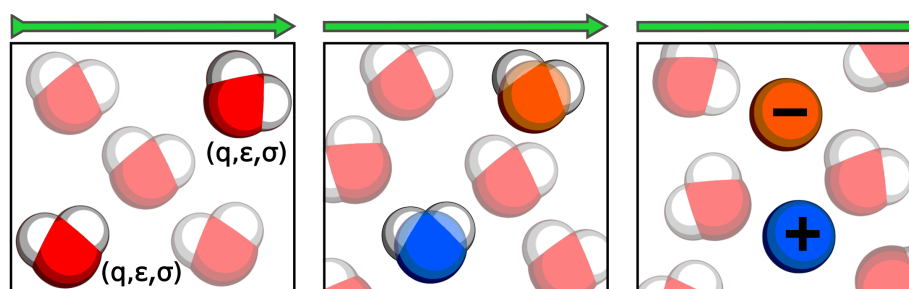


Figure 3. Schematic illustration of the nonequilibrium candidate Monte Carlo (NMC) alchemical protocol used to insert NaCl. Two water molecules are chosen at random for transformation into Na^+ (blue sphere) and Cl^- (orange sphere). Over a number of NMC steps, the nonbonded parameters of each atom in the water molecules, namely the partial charges, q , Lennard-Jones energy well depths, ϵ , and Lennard-Jones separation parameters, σ , are transformed into the nonbonded parameters of the ions along a linear interpolation of the parameters. The hydrogen atoms and extra charge sites (if present) of the water model remain attached to the ions as non-interacting dummy atoms. The entire NMC proposal is then accepted or rejected according to the probability given in equation 56. Note that osmostat NMC moves are mixed with standard Langevin integration at a fixed timestep to obtain fully ergodic sampling. A full description of the Monte Carlo and NMC procedure used here is provided in Appendix 3.

253 the choice of water model, the nonbonded ion parameters are placed on the water oxygen atom, and the
254 hydrogen atoms or additional charge sites (such as in TIP4P) have their nonbonded interactions switched off.
255 The manner in which salt and water are transmuted to one another are is described in Appendix 3. The mass
256 of the ions is set as the same as water, which has no impact on the equilibrium configuration probability
257 density, though it may disrupt the kinetics (which are not of interest here).

258 Nonequilibrium candidate Monte Carlo is used to enhance sampling efficiency
259 A benefit of exchanging ion and water nonbonded forcefield parameters is that this procedure avoids
260 the need to create new cavities in solvent, a difficulty that significantly complicates particle creation and
261 destruction techniques. Nevertheless, instantaneous Monte Carlo attempts to interconvert salt and water
262 will be overwhelmingly rejected as it is highly unlikely that the dipoles of the molecules that surround a
263 transmuted ion—usually solvent—will be orientated in a manner that favorably solvates the new charge.
264 This effect is compounded by the long-range nature of Coulombic interactions. The acceptance probability
265 for salt insertion and deletion would improve drastically if the dipoles and locations of the solvent could be
266 redistributed during an MCMC attempt. Previously, Shelly and Patey developed a configuration bias Monte
267 Carlo technique for the insertion and deletion of ions in grand canonical Monte Carlo²⁹. Their method
268 reorients dipoles in a shell surrounding the inserted or deleted ion, which improved the sampling efficiency
269 by over two orders of magnitude²⁹.

270 Here, we use nonequilibrium candidate Monte Carlo (NMC)³², a technique that is closely related to
271 sequential Monte Carlo and annealed importance sampling^{55,56}, to automatically relax systems around
272 inserted or deleted ions, thereby boosting acceptance rates and sampling efficiencies to values far higher
273 than reported elsewhere.

274 In NMC, a Monte Carlo attempt is divided into a nonequilibrium protocol that drives the system through
275 many intermediate states. Candidate configurations are generated by driving a chosen set of variables
276 (thermodynamic or configurational) through these intermediate states whilst allowing unperturbed degrees
277 of freedom to relax via dynamical propagation in response to the driving protocol. The total amount of work
278 that is accumulated between interleaved steps of perturbation (of the variables of interest) and propagation
279 (of the unperturbed degrees of freedom) is used to accept or reject the candidate configuration. Good NMC
280 acceptance rates can be achieved for a reasonable choice of nonequilibrium protocol; often, a parametric
281 protocol is specified and the total protocol length (or *NMC switching time*) is tuned to be long enough to
282 ensure a system is sufficiently relaxed with respect to the completed perturbation but short enough to be
283 efficient.

284 In our NCMC osmostat, the nonbonded parameters of the ions and water molecules being exchanged
285 are linearly interpolated into a series of equally spaced alchemical states. Each perturbation step along the
286 alchemical path was followed by a fixed number of time-steps of Langevin dynamics where the configurations
287 of the whole system were integrated (see Figure 3). A full description of our Monte Carlo and NCMC procedure
288 is provided in Appendix 3. Here, NCMC propagator uses the same Langevin integrator as used in equilibrium
289 sampling to ensure there was no significant mismatch between the sampled densities. Our particular choice
290 of Langevin integrator (described below) was used to avoid the long correlation times that results from
291 fully Metropolized molecular dynamics integrators and to mitigate the configuration sampling bias that is
292 incurred by unmetropolized finite time-step integrators.

293 We use an integrator that minimizes configuration sampling bias
294 Care must be taken to ensure that the total work is properly accumulated in NCMC, as incorrect accumulation
295 of work or the use of alternative definitions will lead to erroneous computation of the acceptance probability
296 and simulation results. For time reversible MCMC integrators, such as with generalized Hamiltonian Monte
297 Carlo (GHMC), the total work is the *protocol work*: the sum of the instantaneous potential energy changes that
298 result from each perturbation during the driving process⁵⁷. If the system is relaxed in-between perturbations
299 using propagators that do not leave the target distribution invariant, such as unmetropolized Langevin
300 integrators, NCMC can drive systems to undesirable nonequilibrium steady states, whose statistics may
301 differ from equilibrium. On top of the work that is already performed by the driving protocol, propagators
302 that do not satisfy microscopic reversibility can also be considered to perform work on a system⁵⁷. This work,
303 known as the *shadow work*, must either be minimized or eliminated (i.e., via Metropolizing the dynamics) for
304 NCMC to sample very close to, or exactly, from the target probability density.

305 The issue of shadow work accumulation is not limited to propagators in NCMC. Indeed, *all* finite time-
306 step molecular dynamics integrators incur a discretization error that results in biased sampling when
307 used without metropolization. While configuration sampling errors do not occur with GHMC, the correct
308 acceptance criterion requires that the momenta of all particles are reversed upon rejection (or acceptance)
309 of a proposal. The reversal of momenta results in a simulation ‘retracing its steps’, thereby significantly
310 increasing correlation times and decreasing sampling efficiencies. Hamiltonian Monte Carlo sampling
311 can suffer from even longer correlation times, as momenta are randomized for each trial, irrespective of
312 whether the previous move was accepted or not. This problem can be mitigated by using GHMC reduced
313 momentum flipping schemes that still rigorously sample from the target distribution^{58–60}. Correlation times
314 are minimized by GHMC schemes that do not reverse momenta at all, although this incurs sampling bias⁶¹.

315 Recently, Leimkuhler and Matthews have proposed an unmetropolized Langevin dynamics technique that
316 incurs minimal configuration sampling bias⁶². The minimal error is achieved using a particular numerical
317 scheme to update the positions and momenta at each time-step. Denoting half time-step velocity updates as
318 V , half time-step position updates as R , and the addition of an Ornstein-Uhlenbeck process as O (the Brownian
319 motion “kick”), the symmetry in the VRORV splitting scheme leads to a particularly favorable cancellation of
320 configuration sampling error. Leimkuhler and Matthews also found that than VRORV exhibited the lowest
321 error on configuration dependent quantities, such as the potential energy, in biomolecular simulations
322 compared to other symmetric splittings. As Langevin dynamics with VRORV splitting samples very closely
323 to the true configuration Hamiltonian, we expect its neglect within NCMC moves designed to sample
324 configurational properties to induce very little error in sampled configurational densities. For this reason, we
325 used the protocol work to accept or reject proposals from NCMC in our osmostat.

326 Salt concentration and ionic strength

327 Ionic strength influences the effective salt concentration

328 We are interested in quantifying the variation of the instantaneous salt concentration c in our osmostated
329 biomolecular simulations, where

$$c(x, \theta) = \frac{1}{V(x)} N_{\text{NaCl}}(\theta). \quad (20)$$

330 Although the salt concentration of the saline reservoir, i.e. the macroscopic concentration, is known precisely
331 and controlled by the user, the presence of a biomolecule in a simulation, along with any neutralizing
332 counterions, may lead to significant differences in the mean salt concentration in the simulation volume
333 from the macroscopic salt concentration. In contrast, the mean salt concentration in an initially pure box of
334 water should match the macroscopic salt concentration of the reservoir if the chemical potential used in the
335 osmostat is accurately calibrated.

336 The Debye-Hückel theory of electrolytes provided an early, analytical treatment of dilute ionic solutions
337 using continuum electrostatics. In Debye-Hückel theory, the ionic strength I of a system, which for our
338 simulations is

$$I(x, \theta) = \frac{1}{2} \frac{1}{V(x)} \left(z^2 + \sum_{i=1}^N \theta_i^2 \right), \quad (21)$$

339 is used to predict how the effective concentrations, or activities, of ions are affected by the presence
340 of electrolytes in the solution. The key insight of Debye-Hückel theory is that—because of electrostatic
341 screening—the ionic strength tempers the activity of ions, such that increasing the ionic strength of a solution
342 lowers the effective concentration of electrolytes. Although Debye-Hückel theory is too simplistic to be
343 used to accurately predict the salt concentration in biomolecular simulations, the ionic strength may still
344 provide insight into the salt concentrations that we will observe in our osmostated simulations. Thus, we will
345 investigate the variation of the ionic strength as well as the salt concentration. As a large charge number of
346 the biomolecule z will dominate I for small simulation volumes, we will also consider the variation of ionic
347 strength of the solvent only, i.e., by neglecting z^2 in equation 21.

348 Simulation packages add different amounts of salt

349 There is diversity in the way that current practitioners of all-atom biomolecular simulations add salt (*salinate*)
350 to systems during the preparation stages of simulations. While it is common that only neutralizing counterions
351 are added, a number of workflows elect not to add counterions at all²³. Salt pairs may be added, or not
352 added at all, and when they are added, simulation packages use differing definitions of salt concentration,
353 such that each package can add different numbers of salt pairs to the same system even if the desired
354 salt concentration is the same. All packages ignore the presence of neutralizing counterions when adding
355 salt. In this study, we are concerned with quantifying the accuracy of some of the most popular salination
356 techniques.

357 Given a target salt concentration of c_t , a popular method to add salt—exemplified by the Gromacs
358 package¹⁷—uses the initial volume of the system $V(x_0)$ to count the required number of pairs. We determine
359 the number of salt pairs that would be added by this strategy as

$$\hat{N}_{\text{NaCl}}^V = \lfloor V(x_0) c_t \rfloor, \quad (22)$$

360 where $\lfloor y \rfloor$ denotes the floored value of y . We are interested in assessing the accuracy of the corresponding
361 concentration of salt $\hat{c}_V(x) = \hat{N}_{\text{NaCl}}^V / V(x)$. Preparation tools such as CHARMM-GUI¹⁸ add salt based on the
362 initial volume of the *solvent* $V(x_{0,\text{H}_2\text{O}})$, which we reproduce with

$$\hat{N}_{\text{NaCl}}^S = \lfloor V(x_{0,\text{H}_2\text{O}}) c_t \rfloor, \quad (23)$$

363 to estimate the corresponding concentration $\hat{c}_S(x) = \hat{N}_{\text{NaCl}}^S / V(x)$ that would occur for all later configurations.
364 Estimates that use strategies similar to equations 22 and 23 are sensitive to initial volume of the system; if
365 salt is added before the volume is sufficiently equilibrated, the salt concentration during the simulation can
366 deviate significantly from the target concentration. In contrast, packages such as OpenMM^{19,20}, use the *ratio*
367 of salt pairs to water molecules in bulk solvent to add

$$\hat{N}_{\text{NaCl}}^R = \left\lfloor \frac{N_{\text{H}_2\text{O}}}{\hat{c}_{\text{H}_2\text{O}}} c_t \right\rfloor, \quad (24)$$

368 salt pairs, where $\hat{c}_{\text{H}_2\text{O}}$ is concentration of bulk water, for which 55.4 M is used by OpenMM. The corresponding
369 salt concentration $\hat{c}_R(x) = \hat{N}_{\text{NaCl}}^R / V(x)$, as well as $\hat{c}_V(x)$ and $\hat{c}_S(x)$ will be compared to the concentration of salt
370 that results from the application of our osmostat to help inform future simulation strategies.

371 Simulation details

372 Systems considered in the study

373 The primary aims of this study are to quantify and understand how the concentration of salt and ionic
374 strength vary around typical biomolecules, to assess the accuracy of methods that insert salt in typical
375 simulation strategies, and to ascertain whether an NCMC osmostat can decorrelate biomolecule:ion interac-
376 tions faster than fixed-salt dynamics. To meet these aims, we considered four biological systems that are
377 representative of those that are commonly simulated with molecular dynamics: pure water, dihydrofolate
378 reductase (DHFR), the *apo* kinase Src, and the Drew-Dickerson B-DNA dodecamer palindromic sequence.
379 All systems were taken from the OpenMMTools [0.11.1] set of test systems⁶³, such that each system has a
380 different provenance.

381 Dihydrofolate reductase (DHFR) is a small, globular enzyme that has frequently been used as a model
382 system in molecular simulations. The DHFR structure used here was taken from the joint Amber-CHARMM
383 (JAC) benchmark (obtained from the Amber 14 benchmark archive⁶⁴). The protein structure was stripped
384 of hydrogen atoms, and using `tleap`⁶⁵, was re-protonated at pH 7 and solvated in an orthorhombic box
385 of TIP3P waters that had a clearance of at least 10 Å. The Amber 14SB forcefield from the AmberTools 16
386 package was used for the protein⁶⁵. As an initial relaxation of the system, the solvated system was minimized
387 and propagated for 3 ps with Langevin dynamics.

388 The tyrosine kinase Src, a member of the non-receptor tyrosine kinase family, was selected for this
389 study as an example of a prototypical drug target. The *apo* Src structure was taken from the OpenMMtools
390 `testsystems` data set and resolvated with TIP3P in an orthorhombic box that was at least 10 Å away from the
391 protein. As part of the preparation, the energy of system was minimized and subsequently relaxed using 3 ps
392 of Langevin dynamics to remove any bad contacts. Further equilibration was performed as detailed below.
393 The original system was not suitable for simulation with the osmostat as fixed neutralizing counterions
394 were present in the system. The OpenMMtools structure was downloaded from the Protein Data Bank,
395 identification code 1YI6, and prepared using PDBFixer⁶⁶ and protonated at pH 7. The small molecule in the
396 binding site was also removed during the preparation. The Amber 14SB forcefield from the AmberTools 16
397 package was used for the simulations⁶⁵.

398 The Drew-Dickerson dodecamer (CGCGAATTGCGC) is a classic model DNA system. The B-DNA structure
399 of the Drew-Dickerson dodecamer was downloaded from the Protein Data Bank (identification code 4C64).
400 The structure was stripped of ions and solvated in a box of TIP3P water to ensure at least 9 Å of clearance
401 around the DNA. To test the effect of the amount of solvent on the distribution of salt and ions, the structure
402 was also solvated in a box of TIP3P water that had a clearance of at least 16 Å around the DNA. As with
403 the *apo* kinase Src, the system was energy minimized and subsequently relaxed using 3 ps of Langevin
404 dynamics. As described below, further equilibration was also performed. The Amber OL15 forcefield from
405 the AmberTools 16 package was used for the DNA⁶⁷.

406 General simulation details

407 Simulations were performed with OpenMM [7.1.0]²⁰. The osmostat was implemented within the open-source
408 package SaltSwap [0.5.2] that was written for the purpose of this publication. Simulations utilized either
409 TIP3P⁴² or TIP4P-Ew⁴³ water models, and Joung and Cheatham parameters were used for Na⁺ and Cl⁻ ions⁶⁸.
410 Unless otherwise stated, the amount of salt in a simulation was initialized by salinating the system according
411 to equation 24 with the macroscopic concentration as the target concentration c_t .

412 For all simulations, long-range electrostatic interactions were treated with particle mesh Ewald (PME),
413 with both direct-space PME and Lennard-Jones potentials making use of a 10 Å cutoff; the Lennard-Jones
414 potential was switched to zero at the cutoff over a switch width of 1.5 Å to ensure continuity of potential
415 and forces. PME used a relative error tolerance of 10^{-4} at the cutoff to automatically select the α smoothing
416 parameter, and the default algorithm in OpenMM was used to select Fourier grid spacing (which selected a
417 grid spacing of ~ 0.8 Å in each dimension). All bonds to hydrogen were constrained to a within a fractional
418 error of 1×10^{-8} of the bond distances using CCMA^{69,70}, and waters were rigidly constrained with SETTLE⁷¹.
419 OpenMM's long-range analytical dispersion correction was used to avoid pressure artifacts from truncation of

420 the Lennard-Jones potential. Simulations were run at 300 K with a Monte Carlo barostat with 1 atm external
421 pressure and Monte Carlo update interval of 25 steps. Equilibrium and NCMC dynamics were propagated
422 using high-quality Langevin integrators taken from the OpenMMTools [0.11.1] package, with a 2 fs timestep
423 and collision rate of 1 ps^{-1} . Integrators used deterministic forces and OpenMM's mixed single and double
424 precision implementation. In addition to the dynamics used to prepare the systems, every simulation was
425 briefly thermalized using 4 ps of dynamics. Where stated, additional simulation data was discarded from the
426 start of simulations using the automatic procedure in the pymbar timeseries module as detailed in⁷². As
427 described above, positions and velocities were updated using the VRORV splitting scheme (also known as
428 BAOAB) to mitigate the configuration space error in equilibrium sampling and NCMC proposals that result
429 from unmetropolized Langevin dynamics⁶².

430 The insertion or deletion of salt was attempted every 4 ps using the procedure described in Appendix 3.
431 All ions used the same number of atoms, topology, and geometry as the water model used in the simulation.
432 As illustrated in Figure 3, the "insertion" of an ion was achieved by switching the nonbonded parameters of
433 the water oxygen atom to either Na^+ or Cl^- and by simultaneously switching the nonbonded parameters
434 of the water hydrogen atoms (along with any extra charge sites) to zero—the "deletion" of an ion involved
435 the reverse procedure. With the exception of the simulations where the NCMC protocol was optimized, the
436 NCMC protocol was 20 ps long, and consisted of 1000 perturbation steps, where each perturbation followed
437 by 10 steps of Langevin integration with a 2 fs timestep. The pseudo-code for the entire NCMC osmostat,
438 including how it is combined with molecular dynamics can also be found in Appendix 3. Unless otherwise
439 stated, the NCMC protocol length is not accounted for in the reported lengths of the simulations.

440 The simulations were analyzed with open source scripts that used a combination of numpy 1.13.1⁷³,
441 scipy 0.19.1⁷⁴, pymbar 3.0.1⁷⁵, MDTraj 1.8.0⁷⁶, VMD 1.9.4⁷⁷ (see *Code and data availability*); the `saltswap`
442 conda package provided automatically installs the dependencies needed to run the simulation scripts. Plots
443 and figures were produced using Matplotlib 2.0.2⁷⁸ and Inkscape 0.91.

444 **Calibration of the chemical potential**

445 The chemical potential was calibrated in cubic boxes of TIP3P water and TIP4P-Ew water. Both boxes initially
446 had edge lengths of 30 Å with water molecules at roughly the same density as bulk water; the box of
447 TIP3P water contained 887 molecules and the box of TIP4P-Ew water contained 886 molecules. Ten 80 ns
448 SAMS simulations were performed on each box, and were targeted to sample uniformly over salt pairs
449 $N_{\text{NaCl}}(\theta) \in \{0, 1, \dots, 20\}$. The insertion or deletion of salt was attempted every 4 ps. Half of the simulations were
450 initialized with 0 salt pairs, whereas the other half were initialized with 20 salt pairs. The maximum number
451 of salt pairs $N_{\text{NaCl}, \text{max}}$ was chosen to be 20 in these calibration simulations because the corresponding
452 salt concentration (roughly 1.2 M) is beyond the concentrations in biological microenvironments that are
453 typically considered. (Note that the maximum amount of 20 salt pairs applies only to these calibration
454 simulations—the osmostat simulations with solutes have no such maximum number of salt pair limitation.)
455 The volumes of the boxes at each salt occupancy were recorded during the SAMS simulations in order to
456 estimate $\langle V \rangle_{N_{\text{NaCl}}, N, p, T}$ (henceforth abbreviated as $\langle V \rangle_{N_{\text{NaCl}}}$). The SAMS simulation procedure automatically
457 provides on-line estimates of the free energies $f(N_{\text{NaCl}})$, which, along $\langle V \rangle_{N_{\text{NaCl}}}$, are required to calibrate
458 the chemical potential. The protocol work from all of the NCMC insertion and deletion attempts were
459 post-processed with BAR (using the pymbar package⁷⁵) to provide additional estimates of $f(N_{\text{NaCl}})$ along
460 with statistical uncertainties.

461 To assess whether $f(N_{\text{NaCl}})$ and $\langle V \rangle_{N_{\text{NaCl}}}$ had been accurately calculated, larger boxes of TIP3P and TIP4P-
462 Ew water were simulated for 32 ns at a range of chemical potentials $\Delta\mu$. The mean salt concentrations from
463 the simulations were compared to concentrations predicted using equation 19 with the estimated values for
464 $f(N_{\text{NaCl}})$ and $\langle V \rangle_{N_{\text{NaCl}}}$. The boxes of these validation simulations were initially 50 Å in length, and contained
465 4085 TIP3P and 4066 TIP4P-Ew water molecules. These simulations were initialized without any salt present
466 in the systems.

467 **Optimization of the NCMC protocol**

468 We consider only two parameters in optimizing the nonequilibrium protocol used in NCMC proposals: the
469 total number of times the potential is perturbed, T , and the number of Langevin steps that occur before
470 and after each perturbation, K . Generally, we expect the acceptance probability to increase as the overall
471 perturbation is broken into smaller pieces—as T increases. Increasing the number of propagation steps
472 following each perturbation, K , also improves the acceptance probability in a manner that is dependent on
473 the computational efficiency details of the simulation code. To quantify the trade-off between acceptance
474 probability and compute time, we define the NCMC efficiency $E(T, K)$ as

$$E(T, K) = \frac{\langle A \rangle(T, K)}{C(T, K)}, \quad (25)$$

475 where $\langle A \rangle(T, K)$ is the average acceptance probability and $C(T, K)$ is the average computer time per inser-
476 tion/deletion attempt. All simulations were performed and timed on single Nvidia GTX-1080 GPUs. The total
477 protocol length of an NCMC attempt is equal to $T \times K$ multiplied by the Langevin integration timestep, which
478 is 2 fs in this case.

479 Simulations using various NCMC protocols lengths were performed on cubic boxes of TIP3P and TIP4P-Ew
480 that had initial edge lengths of 30 Å. The simulations sampled configurations for a total of 32 ns (excluding the
481 NCMC sampling) and had NCMC protocol lengths up to 40 ps for different combinations of total perturbation
482 steps T and propagation steps K . The insertion or deletion of salt was attempted every 4 ps, such that there
483 were a total of 8000 insertion/deletion attempts for each simulation. The efficiency of each protocol E was
484 estimated relative the efficiency of instantaneous insertion and deletion. Shelly and Patey also used the ratio
485 of the average acceptance probability to the compute time to estimate the efficiency of their configuration
486 bias ion insertion scheme relative to instantaneous insertions²⁹. In this work, no effort was made to optimize
487 the alchemical path.

488 **Quantifying the scaling behavior of the osmostat**

489 To investigate the sampling efficiency of our osmostat under physiological conditions, DHFR was simulated
490 with macroscopic concentrations of 100 mM, 150 mM, and 200 mM. Each simulation was 30 ns long and
491 there were three repeats per macroscopic concentration. Equation 24 was used to add an initial amount
492 of salt to the simulation. The `timeseries` module in `pymbar`⁷⁵ was used to estimate the autocorrelation
493 function of salt concentration as well as the integrated autocorrelation time for each macroscopic salt
494 concentration.

495 It is important to establish how the distributions of salt concentration and salt numbers scale with the
496 number of water molecules in the system and the macroscopic concentration. To this end, we simulated
497 different sizes of water boxes with macroscopic concentrations of 100 mM, 150 mM, and 200 mM. Each
498 simulation was repeated three times.

499 **Estimating the efficiency of ion configuration sampling with NCMC**

500 Ponomarev et al. previously used the Drew-Dickerson DNA palindromic sequence to quantify the rate of
501 convergence of spatial ion distributions in DNA simulations²⁵. Three osmostated simulations and three
502 fixed-salt simulations of the Drew-Dickerson dodecamer were performed for 60 ns with a macroscopic salt
503 concentration of 200 mM. As the insertion or deletion of salt was attempted every 4 ps, there was a total of
504 15,000 attempts. The fixed salt simulations used the same ion topologies and masses as those used by the
505 osmostat, are were added to the system using the scheme summarized by equation 24. The autocorrelation
506 of ion:phosphate interaction occupancies were estimated from the osmostated and fixed-salt simulations
507 using the open-source analysis scripts that accompany this manuscript.

508 **Quantifying the salt concentration around biomolecules**

509 Three 30 ns simulations of *apo* Src kinase were performed, with salt insertion or deletion attempted every
510 4 ps, using a macroscopic concentration of 200 mM. The amount of salt that was initially added to this
511 system was calculated using equation 24. These simulations, as well as those of TIP3P water, DHFR, and the

512 DNA dodecamer described above, were used to analyze the distributions of salt concentration (equation 20),
513 ionic strength (equation 21), and the concentrations of salt that would occur for the heuristic salination
514 schemes described in equations 22, 23, and 24.

515 To further understand the scaling behavior of the distributions of salt concentration with system size, and
516 to assess the extent of finite size effects on the ion spatial distributions around DNA, additional simulations
517 were performed on DNA. The Drew-Dickerson DNA dodecamer was resolvated in a box of TIP3P water that
518 was at least 16 Å away from the molecule. Three repeats of 45 ns long osmostated and fixed-salt simulations
519 were performed, with the insertion or deletion of salt was attempted every 4 ps. The salt concentration
520 distribution was estimated, as were the Na⁺ and Cl⁻ spatial distributions around the DNA.

521 Results

522 SAMS simulations and BAR estimates accurately capture salt insertion free energies.

523 In order to estimate the chemical potential $\Delta\mu$ corresponding to a desired macroscopic salt concentration,
524 we must have precise estimates of both free energies to insert salt into a box of water containing N_{NaCl}
525 salt molecules, $f(N_{\text{NaCl}})$, and the average saline box volume as a function of N_{NaCl} , $\langle V \rangle_{N_{\text{NaCl}}}$, for $N_{\text{NaCl}} \in$
526 $\{0, 1, \dots, N_{\text{NaCl, max}}\}$. Figure 4 (upper left) depicts the computed relative free energy difference for inserting an
527 additional salt pair into a box of water molecules already containing N_{NaCl} salt molecules for both TIP3P and
528 TIP4P-Ew for $N_{\text{NaCl}} \in \{0, \dots, 19\}$. The relative free energies were estimated with BAR using all nonequilibrium
529 work values for salt pair insertion/deletion NCMC proposals, irrespective of whether the proposal attempt
530 was accepted or not, from ten SAMS simulation. Although SAMS also provides *online* estimates for $f(N_{\text{NaCl}})$
531 over this same range³⁵, these online estimates were found to have significantly higher variance than the
532 BAR estimates (see Figure A5.1), so we make use of BAR-derived estimates of $f(N_{\text{NaCl}})$ derived from SAMS
533 simulations throughout.

534 The primary accuracy of the calibration simulations lies in their ability to reproduced desired salt con-
535 centrations in bulk water. Nevertheless, it is encouraging to note that calculated free energy to insert one
536 NaCl pair in a box of TIP3P and TIP4P-Ew are broadly in agreement with previous computational estimates
537 and experimental measurements. As implied by equation 16, the free energy to insert the first salt pair,
538 $\Delta f(N_{\text{NaCl}} = 0)$, can be expressed as the difference in hydration free energy between NaCl and two water
539 molecules. Assuming the hydration free energy of TIP3P and TIP4P-Ew water to be -6.3 kcal/mol⁷⁹, we
540 estimate the hydration free energy of NaCl to be -171.73 ± 0.04 kcal/mol and -170.60 ± 0.04 kcal/mol in
541 TIP3P and TIP4P-Ew water, respectively. Using a different treatment of long-rang electrostatics but same
542 ion parameters as this study, Joung and Cheatham calculated the individual hydration free energies of Na⁺
543 and Cl⁻ in TIP3P and TIP4P-Ew, which can be summed to approximate the hydration free energy of NaCl⁶⁸.
544 These hydration free energies (-178.3 kcal/mol in TIP3P -177.7 kcal/mol in TIP4P-Ew) are within 5% of our
545 estimates. For comparison, estimates of standard NaCl hydration free energies based on experimental data
546 are -170.4 kcal/mol⁸⁰, -171.8 kcal/mol⁸¹, and -177.8 kcal/mol⁸².

547 The chemical potential for a macroscopic salt concentration can be reliably determined
548 The salt insertion free energies and average volumes in Figure 4 *upper left* provide a way to relate the
549 chemical potential $\Delta\mu$ to macroscopic salt concentration $\langle \hat{c} \rangle$ via equation 19. Figure 4 *upper right* shows the
550 predicted macroscopic salt concentration for a range of chemical potentials $\Delta\mu$ computed using equation 19.
551 The average salt concentration in a saline box $\langle c \rangle$ should equal the predicted macroscopic concentration
552 for sufficiently large saline boxes if the chemical potential has been properly calibrated. To verify the
553 accuracy of the calculated values for $f(N_{\text{NaCl}})$ and $\langle V \rangle_{N_{\text{NaCl}}}$, simulations of water boxes, that initially had no
554 salt present, were performed using an osmostat with different fixed chemical potentials and the average salt
555 concentrations in the simulations were estimated (Figure 4; *upper right*). These boxes of TIP3P and TIP4P-Ew
556 waters contained 4085 and 4066 molecules respectively, whereas the TIP3P and TIP4P-Ew boxes used to
557 estimate $f(N)$ and $\langle V \rangle_{N_{\text{NaCl}}}$ contained 887 and 886 molecules respectively. As Figure 4 *upper right* shows, the
558 macroscopic concentrations $\langle \hat{c} \rangle$ predicted using equation 19 fall within the statistical error of the average
559 concentrations $\langle c \rangle$ determined from the fixed- $\Delta\mu$ simulations.

560 Although $\Delta\mu$ is the thermodynamic control parameter for osmostated simulations, experimental wetlab
561 conditions instead generally specify the macroscopic salt concentration $\langle\hat{c}\rangle$ rather than $\Delta\mu$. As the relationship
562 between $\Delta\mu$ and $\langle\hat{c}\rangle$ is monotonic, as illustrated by Figure 4 *upper right*, we can numerically invert equation 19
563 to enable practitioners to choose the desired macroscopic salt concentration and extract the required $\Delta\mu$ for
564 the osmostat to model equilibrium with the macroscopic salt concentration $\langle\hat{c}\rangle$.

565 The average salt concentration is highly sensitive to chemical potential
566 The macroscopic salt concentration $\langle\hat{c}\rangle_{\Delta\mu}$ for a fixed chemical potential $\Delta\mu$ is a highly sensitive and non-
567 linear function of the chemical potential (Figure 4; *upper right*) for both water models. Small changes to
568 the chemical potential, on the order of $1 kT$, can alter the mean concentration by hundreds of millimolar.
569 Correspondingly, to accurately model a given macroscopic concentration c , the function $\Delta\mu(c)$ must be very
570 precisely calibrated.

571 Different water models have distinct chemical potentials for the same salt concentration
572 Strikingly, both the value and shape of $\langle\hat{c}\rangle_{\Delta\mu}$ is very sensitive to choice of water model (Figure 4; *upper*
573 *right*). For instance, a $\Delta\mu$ of about $316 kT$ results in a mean salt concentration in TIP3P water that is
574 approximately 500 mM, compared to approximately 200 mM in TIP4P-Ew water for the same value of $\Delta\mu$.
575 These features highlight the importance of specifically calibrating the chemical potential for each water and
576 ion model as well as estimating $f(N_{\text{NaCl}})$ and $\langle V \rangle_{N_{\text{NaCl}}}$ to a sufficient degree of precision. Figure A5.2 shows
577 that for TIP3P and the treatment of long-rang interactions used herein, the free energies $f(N_{\text{NaCl}})$ for each
578 $N_{\text{NaCl}} \in \{0, 1, \dots, 20\}$ need to be determined to a standard error of 4 kcal/mol to consistently determine the
579 macroscopic concentration to an inaccuracy of at least about 80 mM for $1 \text{ mM} \leq \langle\hat{c}\rangle \leq 1000 \text{ mM}$. The average
580 standard error achieved in the calibration simulations for the free energies $f(N_{\text{NaCl}})$ is 0.02 kcal/mol, which
581 determines the concentration to an inaccuracy no larger than about 1 mM.

582 NCMC greatly enhances the sampling efficiency of salt insertion and deletion moves
583 We estimate that instantaneous salt insertion and deletion moves have acceptance probabilities of 3.0×10^{-51}
584 [95% CI: 5.0×10^{-66} , 9.0×10^{-51}] and 1.0×10^{-46} [95% CI: 3.0×10^{-64} , 4.0×10^{-46}] in TIP3P and TIP4P-Ew water
585 respectively, implying that the implementation of an osmostat is practically impossible using such naive
586 moves. In contrast, we found that in our longest protocol, NCMC insertion/deletion attempts achieved
587 acceptance probabilities of about 30% in TIP3P water and approximately 15% in TIP4P-Ew water (see the
588 lower left of Figure 4). Although the acceptance probability increases monotonically with the length of the
589 protocol, so does the computational cost and time for each attempt. The efficiency, defined in equation 25,
590 quantifies the trade-off between the acceptance rate and computational expense. Figure 4 *lower right* shows
591 that NCMC protocols in TIP3P water that are between 15 ps and 30 ps in length are the most efficient
592 for our procedure. For this reason, all subsequent simulations used TIP3P water and a 20 ps long NCMC
593 protocol. In addition, it was found that 10 propagation steps (at 2 fs) between each perturbation was found
594 to be the most computationally efficient for our simulation code SaltSwap [0.5.2] and OpenMM [7.1.0] (see
595 Figure A5.3). Further optimization of the NCMC protocol would be required for NCMC attempts in TIP4P-Ew
596 to achieve sampling efficiencies that are competitive with those in TIP3P water.

597 An NCMC osmostat can rapidly equilibrate the salt concentration in biomolecular systems
598 Figure 5 shows example salt concentration trajectories around DHFR as well as plots of the corresponding au-
599 tocorrelation functions for three biologically plausible macroscopic salt concentrations. The autocorrelation
600 times for the three macroscopic salt concentrations are on the order of 1 ns, implying that our osmostated
601 simulations should be at least tens of nanoseconds long to generate sufficient uncorrelated samples of salt
602 concentrations. Importantly, the magnitude of the instantaneous salt concentration fluctuations increases
603 with the macroscopic salt concentration, which causes an increase in the correlation time as our osmostat
604 implementation proposes the insertion/deletion of one salt pair a at a time. As a result, more attempts
605 are required to explore salt concentration distributions of higher variance. This suggests that inserting or
606 deleting multiple salt pairs in each attempt could improve the sampling efficiency of our osmostat at higher
607 macroscopic salt concentrations, though longer NCMC insertion/deletion protocols would likely be required

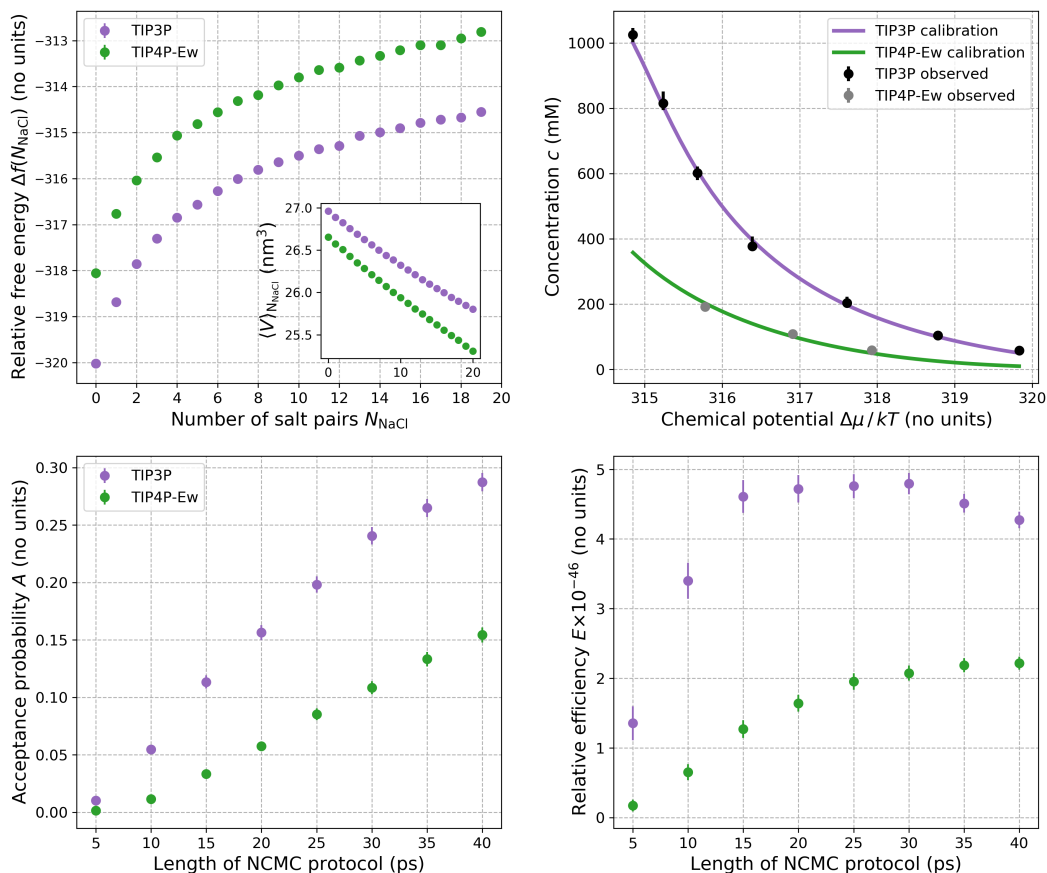


Figure 4. Calibration of chemical potential $\Delta\mu$ for two different water models (TIP3P and TIP4P-Ew) and NCMC protocol optimization. *Top left, main:* The relative free energy $\Delta f(N_{\text{NaCl}})$ —estimated from the SAMS calibration simulations—to insert a Na^+ and Cl^- salt pair and remove two water molecules in boxes of TIP3P and TIP4P-Ew water as a function of the number of salt pairs N_{NaCl} already present in the box (see equation 16). *Top left, inset:* The average volume $\langle V \rangle_{N_{\text{NaCl}}}$ of the saline box as a function of N_{NaCl} , estimated from the SAMS calibration simulations. The TIP3P box contained a total of 887 molecules (including water and ions) and the TIP4P-Ew box contained 886 molecules. The relative free energies and 95% confidence intervals have been calculated using BAR and are smaller than the circular markers. *Top right:* Predicted relationship between the macroscopic salt concentration $\langle c \rangle$ and chemical potential difference $\Delta\mu$ estimated with equation 19 for TIP3P and TIP4P-Ew (dark lines) compared to the average concentrations $\langle c \rangle$ estimated from equilibrium osmostat simulations of boxes of water at specified chemical potentials (circles). There were 4085 and 4066 molecules in the boxes of TIP3P and TIP4P-Ew water, respectively. Bootstrapping of BAR uncertainty estimates of $f(N_{\text{NaCl}})$ and bootstrap uncertainties of $\langle V \rangle_{N_{\text{NaCl}}}$ were used to calculate 95% confidence intervals for the mean concentration curves—these fall inside the thick lines. Error bars on the average simulation concentrations show 95% confidence intervals, and have been estimated using bootstrap sampling of statistically independent subsamples of the simulation concentrations. For the osmostat simulations, equilibration times were automatically estimated and independent samples extracted using the `timeseries` module of `pymbar`⁷⁵. For these osmostat simulations, the shortest and largest estimated equilibration times were 0.2 ns and 26.9 ns respectively, with the largest equilibration time occurring for TIP3P simulation at the lowest $\Delta\mu$ —the starting salt concentration for this simulation was furthest from the equilibrium value. *Bottom left:* Average acceptance probability for salt insertion and deletion as a function of the NCMC protocol length. Simulations were run with a 200 mM osmostat in boxes of TIP3P (887 molecules) and TIP4P-Ew (886 molecules). The mean instantaneous MC acceptance probabilities for TIP3P and TIP4P-Ew are very small: 3.0×10^{-51} [5.0×10^{-66} , 9.0×10^{-51}] and 1.0×10^{-46} [3.0×10^{-64} , 4.0×10^{-46}] respectively, (with 95% confidence intervals denoted in brackets). *Bottom right:* The efficiency (defined by equation 25) of the NCMC protocols relative to instantaneous insertion and deletion attempts in TIP3P for a 200 mM osmostat; all protocols are at least 10^{45} times more efficient than instantaneous insertion and deletion. NCMC protocols of about 20 ps for TIP3P are optimal for our nonequilibrium procedure, though longer protocols are required to achieve similar efficiencies for TIP4P-Ew.

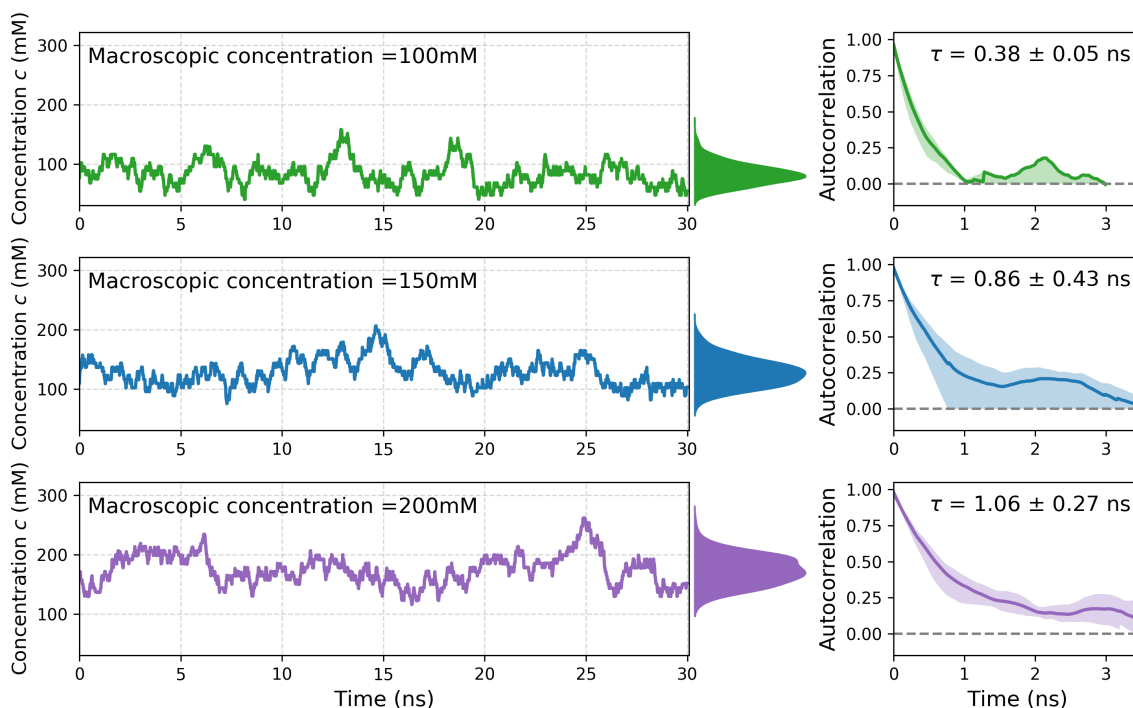


Figure 5. Dynamic salt sampling for DHFR in TIP3P water at three macroscopic salt concentrations. *Left:* Trajectories of the salt concentration in 30 ns simulations of DHFR in a boxes of TIP3P waters as a function of time for 100 mM, 150 mM, and 200 mM NaCl, along with distribution of equilibrium salt concentrations to right of the time-series plots. The distributions were estimated using a Gaussian smoothing kernel with bandwidth of 0.3 mM from all three simulation repeats at each macroscopic concentration. Before the insertion of NaCl, the simulation contained 7023 water molecules. *Right:* Normalized fluctuation autocorrelation functions and integrated autocorrelation times (τ) of salt concentrations for each simulation. Shaded regions and uncertainties on the autocorrelation time signify 95% confidence intervals calculated using bootstrap estimation from three independent simulations.

608 to achieve similar acceptance probabilities.

609 Fluctuation magnitude grows with system size and macroscopic salt concentration

610 Figure 6 *upper left* demonstrates that for a pure box of saline and fixed macroscopic salt concentration,
 611 increasing the number of molecules in the system increases both amount of salt and the spread of the salt
 612 number distribution; in contrast, Figure 6 (*upper right*) reveals that the distribution of the concentration
 613 remains centered around the macroscopic concentration, but the variance decreases. Both of these trends
 614 are to be expected from statistical mechanics (see Appendix 2). The salt concentration distribution for the
 615 smallest water box (with 2094 molecules) in Figure 6 (*upper right*) can be seen to be highly multimodal. Each
 616 peak corresponds a particular number of salt pairs in the system; there are so few water molecules in this
 617 system that changing N_{NaCl} by one results in a large jump in the concentration. Figure 6 (*bottom left and right*)
 618 highlight that for a system with a fixed number of water molecules, the number of salt pairs increases in
 619 proportion with the macroscopic concentration.

620 Salt concentrations vary significantly in typical biomolecular systems

621 Figure 7 shows the distribution of salt concentration and ionic strength for 3 typical biomolecular systems:
 622 DHFR, *apo* Src kinase, and the Drew-Dickerson DNA dodecamer. The distributions in a box of TIP3P are also
 623 shown for reference. The fluctuations of the salt concentration around the macromolecules are substantial:
 624 95% of all salt concentration samples fall within a range of 90.2 mM for DHFR, 87.7 mM for Src kinase, and
 625 135.6 mM for the DNA dodecamer system. We expect these values to be indicative of the natural variation in
 626 salt concentration in the local environments of real biomolecules.

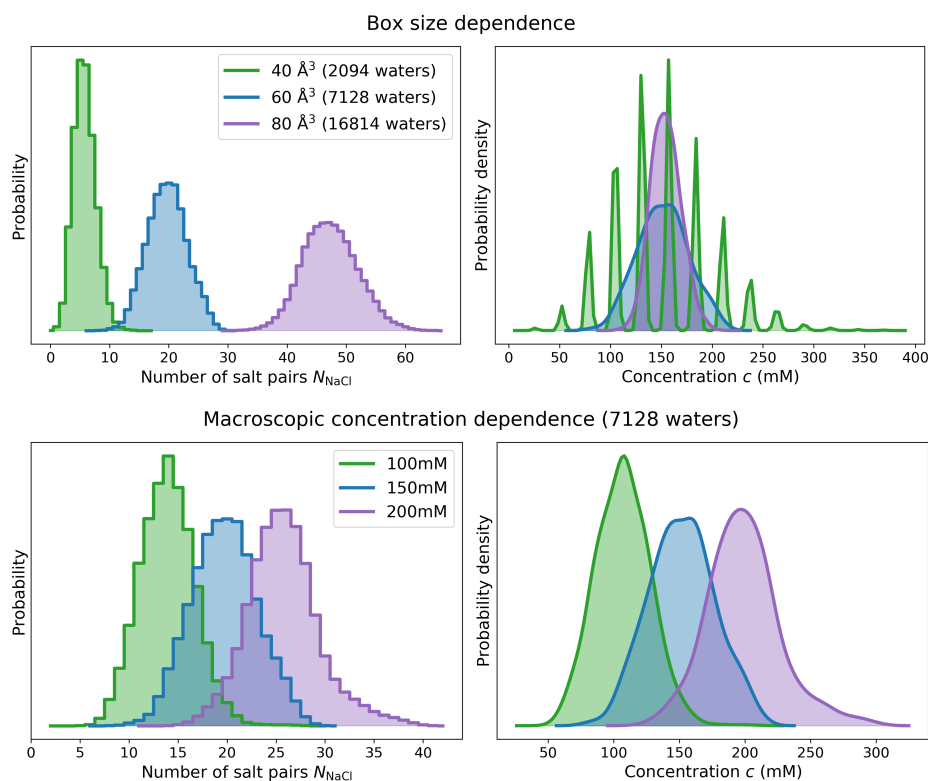


Figure 6. Distribution of salt numbers and concentrations for TIP3P water boxes of varying size and macroscopic salt concentration *Top*: Equilibrium distribution of salt numbers (N_{NaCl} , *left*) and salt concentrations (c , *right*) as a function of the number of water molecules in the simulation. The applied macroscopic concentration was 150mM. blueAs expected (see Appendix 2), at fixed macroscopic salt concentration, the magnitude of fluctuations in the number of salt pairs N_{NaCl} grows with box size (*left*), whereas the magnitude in the concentration decreases with box size. The average salt concentration $\langle c \rangle$ remains fixed at the specified macroscopic concentration (*right*) showing that the calibrated chemical potential $\Delta\mu$ is invariant to box size provided the calibration box is selected to be sufficiently large to avoid finite-size effects. The small range of N_{NaCl} in the 40 Å box results in a multimodal salt concentration distribution. *Bottom*: Equilibrium distribution of salt numbers (N_{NaCl} , *left*) and salt concentrations (c , *right*) as a function of salt concentration for a water box containing 7128 waters.

627 Simulations containing charged biomolecules can experience salt concentrations that deviate
628 systematically from the macroscopic concentrations

629 The DHFR, *apo* Src kinase, and the Drew-Dickerson DNA dodecamer structures have net charges of $-11 |e|$,
630 $-6 |e|$ and $-22 |e|$, respectively. The net charge of the DNA dodecamer is a result of the phosphate group on
631 each of the nucleotides (with each of the eleven phosphate groups carrying $-1 |e|$ charge), whereas the net
632 charges on DHFR and Src kinase are due to an excess of glutamate and aspartate residues over arginine,
633 histidine, and lysine residues. Neutralizing Na^+ ions were added to both systems to avoid the uniform
634 background charge that would be applied automatically with PME electrostatics. Like the other ions in our
635 osmostat, these counterions had transmutable identities.

636 Figure 7 shows that in our osmostated simulations of the macromolecules, the average salt concentration
637 is on average *less* than the macroscopic salt concentration. This is particularly apparent with the DNA
638 dodecamer, which has a mean concentration of 128.0 [121.5, 134.5] mM (where the quantity in brackets
639 denotes the 95% confidence interval of the mean concentration). The salt concentration distribution in
640 the DHFR and Src kinase systems are centered closer to the macroscopic concentration of 200 mM, with
641 estimated means of 174.0 [164.4, 180.4] and 176.3 [171.6, 189.5] mM, respectively. To compute these
642 statistical estimates and confidence intervals, no data was discarded at the start of the simulation, and
643 approximately statistically independent concentration samples were extracted using the pymbar timeseries
644 module⁷⁵.

645 The larger number of water molecules in the Src kinase system is partly the reason why its mean
646 concentration is closer to the macroscopic value than the DNA dodecamer. Bulk-like conditions anchor the
647 sampled salt concentrations about the macroscopic concentration; the more water molecules and salt pairs
648 there are, the smaller the effect a macromolecule has on the salt concentration relative to the whole system.
649 Figure 8 *inset* highlights this phenomenon with the DNA dodecamer; the mean salt concentration moves
650 closer to the macroscopic value when more water molecules are added to the simulation.

651 The accuracy of heuristic salination schemes is system dependent

652 On its own, the excluded volume of the macromolecule will reduce the number of salt pairs that can occupy
653 the simulation volume compared to bulk saline. So, as we define the salt concentration as the number
654 of salt pairs over the total volume of the system (equation 20), one would expect there to be a lower salt
655 concentration than the macroscopic value. The preparation schemes that are typically used to add salt in
656 fixed-salt simulations that account for this effect use either the volume of the solvent (equation 23), or the
657 ratio of the number of salt pairs to water molecules (equation 24). As a result, these methods are closer
658 to the mode of the concentration distributions in the osmostated simulations than the heuristic method
659 that uses the total volume of the system (equation 22). The volume-based methods are sensitive to how
660 equilibrated the volume is when salt is added, and, in Figure 7, the volume at the start of the production
661 simulation was used to estimate the amount of salt that would be added with equations 22 and 23. The
662 salt-water ratio method (equation 24) has no such volume dependence, which is partly why it is a better
663 predictor for the salt concentration than the others.

664 The ionic strength exceeds the salt concentration for charged macromolecules

665 In addition to the distributions of salt concentrations, Figure 7 also shows the ionic strength of the saline
666 buffer. While the ionic strength is used in analytical models to estimate the activities of ionic species⁸³, the
667 only discernible common feature of the ionic strength in our simulations is that it tends to be greater than the
668 salt concentration, which is predominantly due to the presence of neutralizing counterions. The estimated
669 mean ionic strength of the saline buffer in the macromolecular systems are 208.2 [198.2, 213.6] mM for
670 DHFR, 189.0 [179.5, 196.4] mM for Src kinase, and 263.4 [256.6, 269.8] for the DNA dodecamer. It is important
671 to note that the calculated ionic strength can be much larger when the contribution of the macromolecule
672 is included: the estimated ionic strengths for the whole of the DHFR, Src kinase, and DNA systems are
673 551.0 [541.0, 556.4] mM, 263.6 [253.8, 270.8] mM, and 3241.6 [3227.3, 3244.7] mM respectively. These high
674 values, particularly for the DNA system, is because the ionic strength is proportional to the square of the
675 charged number of the ionic solute. It could be more informative to consider the macromolecule and the

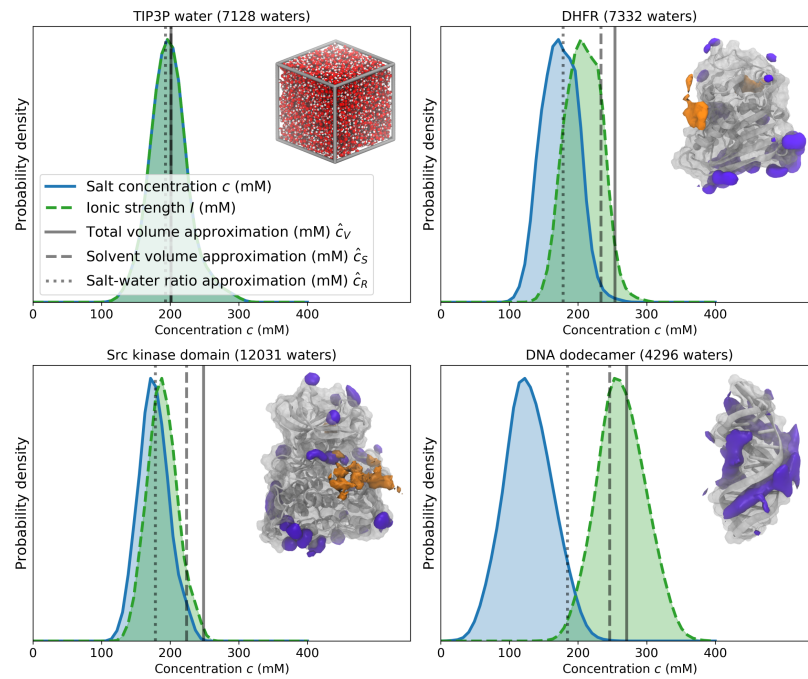


Figure 7. Equilibrium salt concentration distributions for various biomolecular systems simulated with a 200 mM osmostat. Equilibrium salt concentration distributions (blue shaded area) are shown as a kernel density estimate of the probability density, along with the ionic strength of the solvent (light green shaded area with dotted lines). No samples of the salt concentration were discarded for these density estimates. For reference, the mean salt concentrations that would be achieved in three typical fixed-salt salination strategies are shown in transparent gray lines. The continuous line uses equation 22 and the *total* volume of first frame of the production simulation; the dashed line uses equation 23 and the volume of *solvent* at the start of the production simulation, and the dotted line uses equation 24 and the *ratio* of the number of salt pairs and water molecules. Illustrations of each system are also shown in the top right of each plot, with Na⁺ (purple) and Cl⁻ (orange) densities from equilibrium 200 mM osmostat simulations shown around the three macromolecules. Isovalues for the each of 3D ion densities were chosen for visual clarity. *Upper left*: Box of TIP3P waters; *Upper right*: DHFR (dihydrofolate reductase) in TIP3P with isosurfaces containing 14.3% and 0.8% of Na⁺ and Cl⁻ densities, respectively; *Lower left*: *apo* Src kinase in TIP3P with isosurfaces containing 8.5% and 0.6% of the Na⁺ and Cl⁻ densities, respectively; *Lower right*: Drew-Dickerson DNA dodecamer in TIP3P with 8.9% of the Na⁺ density contained in the isosurface.

676 counterions that are bound to it as a single, aggregate macro-ion, such that the contribution to the ionic
 677 strength would be lessened⁸³; however, as there is no clear boundary between bound and unbound ions
 678 (see Figure 8), this approach is conceptually difficult.

679 The osmostat accurately represents the local salt concentration around DNA
 680 The aim of our osmostat is to replicate the local ion concentrations that would occur around biomolecules
 681 when embedded in large saline reservoirs. However, the use of periodic simulation cells and the addition of
 682 neutralizing counterions constrains length scale at which charges are screened (the Debye length) to be less
 683 than or equal to the length scale of the periodic cell. An artificial constriction of the Debye length would
 684 be finite size effect that would limit the accuracy of the salt concentrations from osmostated simulations.
 685 Figure 8 shows the total charge contained within ever increasing distances from the Drew-Dickerson DNA
 686 dodecamer for two simulation box sizes. The smallest box was constructed by solvating the DNA up to a
 687 minimum distance of 9 Å away from the DNA (4296 water molecules), whereas the larger box resulted from
 688 solvating up to a distance of 16 Å from the DNA (9276 water molecules). If the Debye length was significantly
 689 affected by the periodic cell size of the smallest simulation, there would be large discrepancies between the
 690 charge distributions around the DNA of the smallest box and the larger box. Figure 8 indicates that if such
 691 discrepancies exists, they are small, and are not found to be statistically significant in our analysis.

692 Shown first in Figure 7 (lower right), the osmostated simulation of the Drew-Dickerson DNA dodecamer

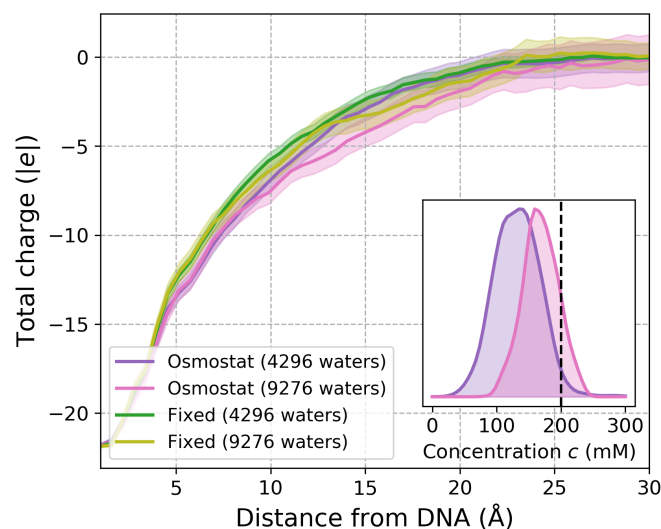


Figure 8. Dependence of the charge screening length and salt concentration on simulation size for the Drew-Dickerson DNA dodecamer. *Main:* The mean total charge within a minimum distance from the Drew-Dickerson DNA dodecamer for 200 mM NaCl osmostated simulations and 200 mM fixed salt fraction simulations. To compare the effect of solvent content on charge screening effects, the DNA dodecamer was solvated in water boxes of two different sizes. The smallest system had water added up to a distance no less than 9 Å away from the DNA dodecamer (adding 4296 waters), whereas the larger was solvated up to a distance at least as large as 16 Å (adding 9276 waters). As each simulation is electrostatically neutral, the total charge must decay to zero as the distance from the DNA dodecamer increases, but the rate at which this decay occurs provides insight into the lengthscales for which biomolecules accrete a neutralizing ion constellation. The charge distributions appear robust with respect to the size of the simulation cell, as all 95% confidence intervals (transparent colors) of the mean charge-distance profiles overlap over all distances considered. The charge-distance profiles were estimated by counting the number of ions within fixed distances of the DNA dodecamer every 1 ns and the confidence intervals were estimated by using bootstrap sampling. *Inset:* Salt concentration probability densities estimated using kernel density estimation for 200 mM osmostated simulations with different amounts of solvent. The simulation with the small solvent box (purple) recruits far fewer salt pairs from bulk on average (dotted black line denotes 200 mM), while the average salt concentration of the simulation with the larger solvent box (pink) is significantly less perturbed from bulk.

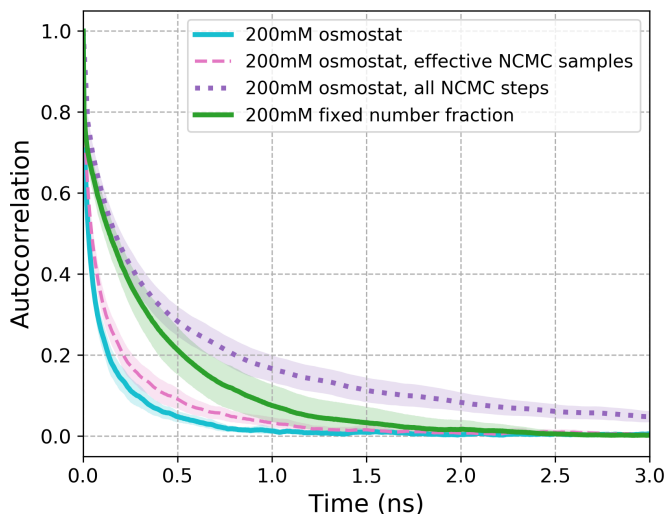


Figure 9. Phosphate-cation normalized fluctuation autocorrelation functions for binary occupancies around a DNA palindrome. The Drew-Dickerson DNA dodecamer (CGCGAATTGCGC) is a palindromic DNA sequence that has been traditionally been used as a demonstration of the slow convergence of ion distributions around the phosphate backbone of DNA. Phosphate-cation normalized fluctuation autocorrelation functions for binary occupancies in standard MD (thick green) and MD with dynamic ion sampling either neglecting the NCMC switching time (thick cyan), or the effective number of samples taken with accepted NCMC moves (dashed pink), or accounting for all NCMC MD steps whether the moves were accepted or not (dotted purple). The latter accounts for the total computational expense of our NCMC protocol. Shaded regions highlight 95% bootstrap confidence intervals, with bootstrap samples taken from all the adenine groups from the three simulations.

693 experienced significantly lower NaCl concentrations than the applied 200 mM macroscopic NaCl concentra-
694 tion. This difference highlights how the local ionic environment of a solute can be strikingly different from
695 bulk saline. Increasing the amount of water in the simulation diminishes the relative effect that DNA has on
696 perturbing the salt concentration distribution of the whole system. Figure 8 (inset), shows that increasing
697 the number of water molecules in the system from 4296 to 9276 molecules partially masks the local salt
698 concentration around the DNA, such that the total salt concentration over the whole system is closer to the
699 macroscopic concentration of 200 mM.

700 The NCMC osmostat can efficiency of ion-biomolecule interactions

701 To compare the computational efficiency of NCMC ion sampling to that of fixed-salt MD simulations, the
702 autocorrelation functions of cation-phosphate interactions were estimated from the DNA dodecamer
703 simulations. Cation-phosphate interactions were recorded as every time a cation was within 5 Å of the
704 phosphorous atoms in adenine nucleotides. This cutoff was chosen following the DNA convergence analysis
705 of Ponomarev et al.²⁵. The autocorrelation function of these interactions measures the probability that a
706 cation that is initially within the distance cutoff will also be present after a given amount of time. As our
707 osmostat uses NCMC to add and remove ions, one would expect the osmostat interaction autocorrelation
708 function to decay significantly faster than that from the fixed salt simulations when only considering the
709 molecular dynamics—Figure 9 shows that this is indeed the case.

710 When the simulation time from NCMC is not considered, the phosphate-cation interaction autocorrelation
711 function from the osmostat simulations decays significantly faster than the fixed salt simulations (Figure 9).
712 The corresponding integrated autocorrelation times for osmostated simulations and fixed-salt simulations
713 are 0.11 [0.09, 0.13] ns and 0.29 [0.23, 0.36] ns respectively. As each accepted NCMC move has propagated
714 the configurations of the whole system, the faster decorrelation of DNA-ion interactions could be a result of
715 these extra propagation steps, as opposed to the fact that ions are being inserted and deleted. As described

716 in the methods, a salt insertion or deletion attempt occurs every 4 ps, and an NCMC attempt involves 20 ps
717 of dynamics. The average acceptance probability in the DNA simulations was calculated to be 11.9 [11.7,
718 12.2] %. Therefore, the osmostated simulations propagate the system $1.6 [\approx (0.119 \times 20 \text{ ps} + 4 \text{ ps})/4 \text{ ps}]$ times
719 as much dynamics than fixed salt simulations. Multiplying the osmostated integrated autocorrelation time
720 by this factor results in a value that remains significantly less than the integrated autocorrelation time from
721 the fixed salt simulations. Figure 9 *right* shows the osmostated autocorrelation function when the timescale
722 has been multiplied by the effective NCMC sampling factor (1.6). Despite the application of this factor, the
723 fixed-salt autocorrelation function can be seen to decay significantly slower than the stretched osmostated
724 autocorrelation function. Thus, the increased sampling efficiency observed in the osmostated simulations
725 cannot be explained by the extra dynamics sampled in the NCMC simulations. This implies that the random
726 insertion and deletion, not the NCMC that was used to enhance the move efficiency, is responsible for the
727 rapid decorrelation of ion interactions observed in the DNA osmostated simulations.

728 The total number of NCMC timesteps (including from rejected moves) can be used to account for the
729 additional computational burden of the NCMC osmostat in the phosphate-cation autocorrelation times.
730 There is an additional 20 ps of dynamics for every insertion/deletion attempt, irrespective of whether
731 the proposal was accepted or not. As each attempted is preceded by 4 ps of equilibrium dynamics, our
732 osmostated simulations have 6 (= $(20 \text{ ps} + 4 \text{ ps})/4 \text{ ps}$) times as timestep evaluations than the fixed-salt
733 simulations. Multiplying the mean integrated autocorrelation time from the osmostat simulations by this
734 factor yields an effective autocorrelation of 0.65 [0.55, 0.75] ns. Although this estimate now exceeds the
735 upper confidence interval of the fixed-salt integrated autocorrelation time (0.29 [0.23, 0.36] ns), there is only
736 approximately 0.1 ns difference between the lower and upper confidence intervals. Figure 9 also shows
737 the osmostat phosphate-ion autocorrelation function when the all the NCMC propagation steps (including
738 rejected moves) are accounted for. One can see that for below ~ 1 ns, the 95% confidence intervals of the
739 autocorrelation functions overlap with those of fixed-salt autocorrelation function. These results imply the
740 dynamic NaCl sampling achieved by our osmostat has a similar cost effectiveness—with regards to ion
741 sampling—than fixed-salt simulations, with the additional benefit of sampling realistic salt concentrations.

742 Discussion

743 In this work, we have implemented an osmostat that dynamically samples the NaCl concentration in
744 biomolecular simulations. The osmostat couples a simulation cell to a saline reservoir at a fixed macroscopic
745 concentration and allows the salt concentration in the simulation to fluctuate about its equilibrium value.
746 We have applied our osmostat to simulations of dihydrofolate reductase (DHFR), *apo* Src kinase, and the
747 Drew-Dickerson B-DNA dodecamer (CGCGAATTGCGC), and found that the mean salt concentration can differ
748 significantly from the amount salt added by common molecular dynamics methodologies. In addition, we
749 found that the salt concentration fluctuations were large, being of the same order of magnitude as the
750 mean. These results show that the ionic composition around biomolecules can be highly variable and system
751 dependent.

752 The insertion and deletion of salt was greatly enhanced by nonequilibrium candidate Monte Carlo (NCMC),
753 to the extent that the protocol used in our simulations was approximately 5×10^{46} times more efficient than
754 instantaneous attempts in TIP3P water. The Drew-Dickerson B-DNA dodecamer is a palindromic sequence
755 that facilitated a study of the convergence of ion distributions around the DNA. We found that, despite the
756 additional computational expense of the NCMC osmostat, the sampling and computational efficiency of
757 DNA:ion interactions remained comparable to fixed-salt simulations. However, it is important to note that
758 made no effort to optimize the NCMC protocols beyond selecting an appropriate total switching time for
759 NCMC moves—it is possible that further optimization of these protocols using recent techniques based on
760 mapping geodesics in the thermodynamic metric tensor space^{84–88} can lead to increased efficiency.

761 Potential applications

762 While the dependence of enzyme-substrate activity on ionic strength is well documented, the impact of salt
763 concentration on protein-ligand binding affinity is much less clear. Recently, Papanephytous et al. performed
764 a systematic analysis on the effect of buffer conditions on the *in vitro* affinity of three complexes¹⁵, finding

765 salt concentration dependence to be system dependent and largest for complexes that formed hydrophilic
766 interactions. Our osmostat provides the opportunity to rigorously study the impact of salt concentration on
767 protein-ligand binding affinities *in silico*. We are interested to know if similar trends to what Papaneophytou
768 et al. observed can be reproduced in all-atom binding free energies calculations, and whether binding free
769 energy estimates differ significantly between simulations carried out with and without an osmostat. Free
770 energy calculations on complexes whose association is sensitive to the concentration of salt are likely to
771 be most affected by the osmostat, given the large fluctuations of concentration and the deviation from the
772 fixed-salt values that occurred in our simulations (see Figure 7). The combination of self adjusted mixture
773 sample (SAMS) and Bennett acceptance ratio (BAR) that we used to calibrate the chemical potential can
774 also be used to estimate the difference between traditional and osmostated free energy calculations. If
775 significant differences between binding free energy calculations in fixed-salt and osmostat simulations are
776 observed, it is also possible to apply the same SAMS-BAR methodology to correct the free energy calculations
777 that have been performed with fixed salt.

778 As our osmostat has been designed to reproduce realistic salt environments around biomolecules, it is
779 well suited to study systems whose function are sensitive to the salt concentration, or biomolecules that
780 are regulated by interactions with Na^+ or Cl^- . While our osmostat can efficiently sample ion binding to
781 biomolecular surfaces, the sampling of deeply buried ion binding sites is likely to be no more than efficient
782 than in typical molecular dynamics simulations due to the fact that our osmostat is implemented by swapping
783 water with salt. To this end, the osmostat could be improved and generalized if position-biased insertions
784 of fully-decoupled ghost molecules could be added to its sampling repertoire. An example of one such
785 biasing scheme can be found in the biomolecular simulation package ProtoMS, where the grand canonical
786 insertion and deletion of water are attempted in a pre-defined region within proteins^{48,49}. Previously, Song
787 and Gunner studied the interplay between protein conformation, residue pKas, and ion binding affinity using
788 a grand canonical ion insertion scheme within the MCE framework⁶. Their work provided structural insight
789 into the often tight-coupling between ion and proton affinity as well as the pH sensitivity of ion binding,
790 and highlights the power of specialized ion sampling schemes to rationalize and understand experimental
791 measurements. The insertion of decoupled ghost molecules—while it would likely require more highly
792 optimized alchemical protocols for insertion—would also permit generalizing the method to more complex
793 salt or buffer molecules or other excipients.

794 Enhancing realism in molecular simulations

795 Because the pKa of protein residues are dependent on the ionic strength of the medium, a natural extension
796 of the osmostat is to combine it with constant-pH simulations in explicit water. Previously, Chen and
797 Roux coupled protonation state changes with the insertion and deletion of ions to maintain electrostatic
798 neutrality^{33,34}. The application of an osmostat to such transformations would allow for the macroscopic
799 ion concentration—as well pH—to be rigorously maintained, and could be implemented in modular MCMC
800 scheme that updates protonation states and ion identities in tandem.

801 This work only considers the concentration of NaCl, but both the formalism we introduce in the Theory
802 section and the flexibility SaltSwap code-base can be readily extended to sample over biologically relevant
803 salt mixtures by including additional monovalent species such as K^+ and divalent species like Ca^{2+} . More
804 complex ions or buffer molecules, such as HCO_3^- would require a more significant extension to code (such as
805 the insertion of ghost particles described earlier), and could be implemented by using a softcore alchemical
806 NCMC pathway that converts the molecule between fully interacting and noninteracting states.

807 The combination of a multicomponent osmostat with a constant-pH methodology would allow for realistic
808 physiological conditions to be better approximated in molecular simulations. While it is well appreciated that
809 pathological tissue can be found with altered pH—tumor microenvironments can have low pH, while cancer
810 cells can have elevated pH, for example⁸⁹—pathologies can also disrupt healthy ion compositions⁵. The
811 ability to reproduce specific ionic concentrations as well as pH would open the possibility of using molecular
812 simulations to target compounds to specific microenvironments or achieve selectivity via salt-dependent
813 environmental differences. Indeed, Spahn et al. recently used molecular simulations to develop an analgesic
814 that selectively targets the μ -opioid receptors in damaged, low pH, tissues⁹⁰.

815 Improving osmostat efficiency

816 We have demonstrated that our implementation of the NCMC osmostat was sufficient to sample equilibrium
817 distributions of ions around biomolecules in practical simulation times. We have not yet extensively optimized
818 the osmostat for computational or algorithmic efficiency beyond exploring NCMC protocol lengths (Figure 4
819 and Figure A5.3), such that there a number of ways that the computational efficiency could be further
820 improved.

821 In our current implementation, which only proposes insertion/deletion of a single salt pair in each
822 proposal, the correlation time for the instantaneous salt concentration increases with increasing system size
823 as the size of the equilibrium fluctuations also grow in terms of total numbers of ions (Figure 5). Inserting
824 or deleting multiple ion pairs—likely using longer specialized NCMC protocols tuned to the number of
825 ions being inserted or deleted—could help maintain efficiency. Adaptive MCMC proposals, currently in
826 widespread use in the Bayesian inference community (e.g., PyMC⁹¹), could be used to automatically tune the
827 number of ions proposed to be deleted or inserted based on the current concentration and the history of
828 the sampler, provided care was taken to ensure the adaptation method maintained ergodicity and ensured
829 the target density was properly sampled⁹². One of the earliest adaptive scheme was originally validated on
830 unimodal distributions⁹³, such that a discretized variant could be well suited to sampling the number of
831 pairs.

832 Acceptance rates can also be increased by using proposals that do not simply select ions at random,
833 but instead select ions that are more easily inserted/deleted based on some rapidly-evaluated surrogate
834 (such as their instantaneous Monte Carlo acceptance probabilities or the electrostatic potential on water
835 and ion sites), provided this biased selection probability is accounted for in a modified Metropolis-Hastings
836 acceptance criteria.

837 There is a great deal of potential to improve the efficiency of the NCMC protocol used for the insertion
838 and deletion proposals. The current work uses a linear interpolation of the salt and water nonbonded
839 parameters as the alchemical path and perturbations steps that are equally spaced with respect to the
840 parameters, primarily because this is the simplest scheme to implement. The only optimization carried out
841 here was tuning the total protocol length to be sufficiently long to achieve high acceptance rates but not
842 so long that the overall efficiency would be diminished by further extending the protocol length (Figure 4).
843 Optimized NCMC protocols can reduce protocol switching times required to achieve high acceptance rates,
844 thereby increasing overall efficiency. The ability to quantify the *thermodynamic length* of the nonequilibrium
845 protocol allows the problem of protocol optimization to be tackled rigorously. The thermodynamic length
846 (an application of the Fisher-Rao metric to statistical mechanics⁹⁴) is a natural, albeit abstract, measure of
847 the distance traversed by a system during a thermodynamic driving process⁸⁴.

848 Within this framework, optimal NCMC protocols are given by geodesics in a Riemannian metric tensor
849 space⁸⁶. The thermodynamic length of the NCMC protocol can be estimated in separate equilibrium
850 simulations spaced along the alchemical path, or estimated directly from the protocol work values of
851 the NCMC switching trajectories, including those from rejected proposals⁸⁵. For optimizing a preselected
852 alchemical path, spacing the perturbation steps to be equidistant with respect to the thermodynamic length
853 can improve acceptance rates by reducing the total variance of the protocol work. As optimal paths are
854 geodesics in thermodynamic space, the most efficient alchemical path for the insertion or deletion will likely
855 be a nonlinear, rather than linear, interpolation of the water and ion nonbonded parameters. Previous
856 efforts to optimize nonequilibrium paths have included directly solving for the geodesic⁸⁷, sampling the
857 protocol from an ensemble⁸⁸, and by restricting the optimization to a family of functional forms⁹⁵. The close
858 relationship between thermodynamic length and the dissipation along the path also suggests that restricting
859 the propagated dynamics to only the first few layers of the solvation shell around the transmuted molecules
860 could also improve the NCMC protocol.

861 Conclusion

862 The philosophy of this work is that increasing the realism of biomolecular simulations will aid structural
863 inference and improve the quantitative accuracy of predictions. We believe that the NCMC osmostat we
864 have presented here will be a useful tool for probing the interactions of ions and biomolecules under more

865 physiological conditions than considered in traditional molecular dynamics simulations. It is our hope that
866 the application of the osmostat to protein-ligand binding free energy calculations and extending the method
867 to more comprehensive ion compositions will improve its utility even further.

868 Code and data availability

- 869 • Code is available at <https://github.com/choderalab/saltswap>
- 870 • Data analysis scripts available at <https://github.com/choderalab/saltswap-results>

871 Acknowledgments

872 GR, ASR, PBG, JF, and JDC acknowledge support from the Sloan Kettering Institute. JDC acknowledges support
873 from NIH grant P30 CA008748. JF acknowledges support from NSF grant CHE 1738979. PBG acknowledges
874 support from Silicon Therapeutics Open Science Fellowship. The authors are especially grateful to Zhiqiang
875 Tan (Rutgers) for many fruitful discussions on the theory and application of self-adjusted mixture sampling
876 and nonequilibrium candidate Monte Carlo, to Marilyn R. Gunner (CCNY) for her insight in counterion
877 distributions around macromolecules, Peter Eastman (ORCID: [0000-0002-9566-9684](https://orcid.org/0000-0002-9566-9684)) for his help and advice
878 with OpenMM, and Kyle A. Beauchamp (ORCID: [0000-0001-6095-8788](https://orcid.org/0000-0001-6095-8788)) for the DHFR system. JDC expresses
879 enormous gratitude to Ken A. Dill (ORCID: [0000-0002-2390-2002](https://orcid.org/0000-0002-2390-2002)) for highly formative conversations about
880 the nature of thermodynamic parameters relevant to biomolecular systems on microscopic lengthscales and
881 his encyclopedic knowledge of the foundational experiments that laid bare their role in driving biophysical
882 phenomena; some of these ideas are realized here.

883 Disclosures

884 JDC is a member of the Scientific Advisory Board for Schrödinger, LLC.

885 References

- 886 [1] Moore, R. D.; Morrill, G. A. A possible mechanism for concentrating sodium and potassium in the cell nucleus. *Biophys.*
887 *J.* **1976**, *16*, 527–533.
- 888 [2] Milo, R.; Phillips, R. *Cell Biology by the Numbers*, draft ed.; Garland Science, 2015; pp 127–130.
- 889 [3] Olaf S., A. *Encyclopedia of Metalloproteins*; Springer, 2013; pp 580–587.
- 890 [4] Le Rudulier, D.; Strom, A. R.; Dandekar, A. M.; Smith, L. T.; Valentine, R. C. Molecular biology of osmoregulation.
891 *Science* **1984**, *224*, 1064–1068.
- 892 [5] Eil, R. et al. Ionic immune suppression within the tumour microenvironment limits T cell effector function. *Nature*
893 **2016**, *537*, 539–543.
- 894 [6] Song, Y.; Gunner, M. R. Using multiconformation continuum electrostatics to compare chloride binding motifs in
895 alpha-amylase, human serum albumin, and Omp32. *J. Mol. Biol.* **2009**, *387*, 840–856.
- 896 [7] Southall, N. T.; Dill, K. A.; Haymet, A. D. J. A view of the hydrophobic effect. *J. Phys. Chem. B* **2002**, *106*, 521–533.
- 897 [8] Hribar, B.; Southall, N. T.; Vlachy, V.; Dill, K. A. How ions affect the structure of water. *J. Am. Chem. Soc.* **2002**, *124*,
898 12302–12311.
- 899 [9] Hofmeister, F. Zur lehre von der wirkung der salze: zweite mittheilung. *Archiv Exp. Path. Pharm.* **1888**, *24*, 247–260.
- 900 [10] Melander, W.; Horváth, C. Salt effects on hydrophobic interactions in precipitation and chromatography of proteins:
901 An interpretation of the lyotropic series. *Arch. Biochem. Biophys.* **1977**, *183*, 200–215.
- 902 [11] Pegram, L. M.; Record, M. T. Hofmeister salt effects on surface tension arise from partitioning of anions and cations
903 between bulk water and the air-water interface. *J. Phys. Chem. B* **2007**, *111*, 5411–5417.
- 904 [12] Hammarsten, O.; Chu, G. DNA-dependent protein kinase: DNA binding and activation in the absence of Ku. *Proc. Natl.*
905 *Acad. Sci.* **1998**, *95*, 525–530.
- 906 [13] Lundbäck, T.; Härd, T. Salt dependence of the free energy, enthalpy, and entropy of nonsequence specific DNA
907 binding. *J. Phys. Chem.* **1996**, *100*, 17690–17695.

- 908 [14] Misra, V. K.; Sharp, K. A.; Friedman, R. A.; Honig, B. Salt effects on ligand-DNA binding. *J. Mol. Biol.* **1994**, *238*, 245–263.
- 909 [15] Papanepoytous, C. P.; Grigoroudis, A. I.; McInnes, C.; Kontopidis, G. Quantification of the effects of ionic strength,
910 viscosity, and hydrophobicity on protein-ligand binding affinity. *ACS Med. Chem. Lett.* **2014**, *5*, 931–936.
- 911 [16] Ong, W.; Kaifer, A. E. Salt effects on the apparent stability of the cucurbit [7] uril- methyl viologen inclusion complex. *J.*
912 *Org. Chem.* **2004**, *69*, 1383–1385.
- 913 [17] Abraham, M. J.; Murtola, T.; Schulz, R.; Páll, S.; Smith, J. C.; Hess, B.; Lindahl, E. GROMACS: high performance molecular
914 simulations through multi-level parallelism from laptops to supercomputers. *SoftwareX* **2015**, *1-2*, 19–25.
- 915 [18] Jo, S.; Kim, T.; Iyer, V. G.; Im, W. CHARMM-GUI: A web-based graphical user interface for CHARMM. *J. Comput. Chem.*
916 **2008**, *29*, 1859–1865.
- 917 [19] Eastman, P.; Friedrichs, M. S.; Chodera, J. D.; Radmer, R. J.; Bruns, C. M.; Ku, J. P.; Beauchamp, K. A.; Lane, T. J.;
918 Wang, L.-P.; Shukla, D.; et al., OpenMM 4: a reusable, extensible, hardware independent library for high performance
919 molecular simulation. *J. Chem. Theory Comput.* **2013**, *9*, 461–469.
- 920 [20] Eastman, P.; Swails, J.; Chodera, J. D.; McGibbon, R. T.; Zhao, Y.; Beauchamp, K. A.; Wang, L.-P.; Simmonett, A. C.;
921 Harrigan, M. P.; Stern, C. D.; et al., OpenMM 7: rapid development of high performance algorithms for molecular
922 dynamics. *PLOS Comput. Biol.* **2017**, *13*, e1005659.
- 923 [21] Darden, T.; York, D.; Pedersen, L. Particle mesh Ewald: An $N \log N$ method for Ewald sums in large systems. *J. Chem.*
924 *Phys.* **1993**, *98*, 10089–10092.
- 925 [22] Hub, J. S.; de Groot, B. L.; Grubmüller, H.; Groenhof, G. Quantifying artifacts in Ewald simulations of inhomogeneous
926 systems with a net charge. *J. Chem. Theory Comput.* **2014**, *10*, 381–390.
- 927 [23] Wang, L.; Wu, Y.; Deng, Y.; Kim, B.; Pierce, L.; Krilov, G.; Lupyán, D.; Robinson, S.; Dahlgren, M. K.; Greenwood, J.; et al.,
928 Accurate and reliable prediction of relative ligand binding potency in prospective drug discovery by way of a modern
929 free-energy calculation protocol and force field. *J. Am. Chem. Soc.* **2015**, *137*, 2695–2703.
- 930 [24] Ravishanker, G.; Auffinger, P.; Langley, D. R.; Jayaram, B.; Young, M. A.; Beveridge, D. L. In *Reviews in Computational*
931 *Chemistry*; Lipkowitz, K. B., Boyd, D. B., Eds.; John Wiley & Sons, Inc.: Hoboken, NJ, USA, 1997; Vol. 11; pp 317–372.
- 932 [25] Ponomarev, S. Y.; Thayer, K. M.; Beveridge, D. L. Ion motions in molecular dynamics simulations on DNA. *Proc. Natl.*
933 *Acad. Sci.* **2004**, *101*, 14771–14775.
- 934 [26] Rueda, M.; Cubero, E.; Laughton, C. A.; Orozco, M. Exploring the counterion atmosphere around DNA: what can be
935 learned from molecular dynamics simulations? *Biophys. J.* **2004**, *87*, 800–811.
- 936 [27] Thomas, D. G.; Baker, N. A. GIBS: A grand-canonical Monte Carlo simulation program for simulating ion-biomolecule
937 interactions. *arXiv:Quantitative Biology* 1704.05534.
- 938 [28] Vitalis, A.; Baker, N. A.; McCammon, J. A. ISIM: a program for grand canonical Monte Carlo simulations of the ionic
939 environment of biomolecules. *Mol. Simul.* **2004**, *30*, 45–61.
- 940 [29] Shelley, J. C.; Patey, G. N. A configuration bias Monte Carlo method for ionic solutions. *J. Chem. Phys.* **1994**, *100*,
941 8265–8270.
- 942 [30] Lísál, M.; Smith, W. R.; Kolafa, J. Molecular simulations of aqueous electrolyte solubility: 1. The expanded-ensemble
943 osmotic molecular dynamics method for the solution phase. *J. Phys. Chem. B* **2005**, *109*, 12956–12965.
- 944 [31] Moučka, F.; Lísál, M.; Škvor, J.; Jirsák, J.; Nezbeda, I.; Smith, W. R. Molecular simulation of aqueous electrolyte solubility.
945 2. Osmotic ensemble Monte Carlo methodology for free energy and solubility calculations and application to NaCl. *J.*
946 *Phys. Chem. B* **2011**, *115*, 7849–7861.
- 947 [32] Nilmeier, J. P.; Crooks, G. E.; Minh, D. D. L.; Chodera, J. D. Nonequilibrium candidate Monte Carlo is an efficient tool for
948 equilibrium simulation. *Proc. Natl. Acad. Sci.* **2011**, *108*, E1009–E1018.
- 949 [33] Chen, Y.; Roux, B. Constant-pH hybrid nonequilibrium molecular dynamics–Monte Carlo simulation method. *J. Chem.*
950 *Theory Comput.* **2015**, *11*, 3919–3931.
- 951 [34] Radak, B. K.; Chipot, C.; Suh, D.; Jo, S.; Jiang, W.; Phillips, J. C.; Schulten, K.; Roux, B. Constant-pH molecular dynamics
952 simulations for large biomolecular Systems. *J. Chem. Theory Comput.* **2017**,
- 953 [35] Tan, Z. Optimally adjusted mixture sampling and locally weighted histogram analysis. *J. Comput. Graph. Stat.* **2017**, *26*,
954 54–65.

- 955 [36] Lyubartsev, A. P.; Martsinovski, A. A.; Shevkunov, S. V.; Vorontsov-Velyaminov, P. N. New approach to Monte Carlo
956 calculation of the free energy: method of expanded ensembles. *J. Chem. Phys.* **1992**, *96*, 1776–1783.
- 957 [37] Bennett, C. H. Efficient estimation of free energy differences from Monte Carlo data. *J. Comput. Phys.* **1976**, *22*,
958 245–268.
- 959 [38] Shirts, M. R.; Bair, E.; Hooker, G.; Pande, V. S. Equilibrium free energies from nonequilibrium measurements using
960 maximum-likelihood methods. *Phys. Rev. Lett.* **2003**, *91*.
- 961 [39] Crooks, G. Excursions in statistical dynamics. Ph.D. thesis, 1999.
- 962 [40] Faller, R.; de Pablo, J. J. Constant pressure hybrid molecular dynamics–Monte Carlo simulations. *J. Chem. Phys.* **2002**,
963 *116*, 55.
- 964 [41] Liu, J. *Monte Carlo strategies in scientific computing*; Springer Series in Statistics; Springer, 2008.
- 965 [42] Jorgensen, W. L.; Chandrasekhar, J.; Madura, J. D.; Impey, R. W.; Klein, M. L. Comparison of simple potential functions
966 for simulating liquid water. *J. Chem. Phys.* **1983**, *79*, 926–935.
- 967 [43] Horn, H. W.; Swope, W. C.; Pitera, J. W.; Madura, J. D.; Dick, T. J.; Hura, G. L.; Head-Gordon, T. Development of an
968 improved four-site water model for biomolecular simulations: TIP4P-Ew. *J. Chem. Phys.* **2004**, *120*, 9665–9678.
- 969 [44] Green, P. J. Reversible jump Markov chain Monte Carlo computation and Bayesian model determination. *Biometrika*
970 **1995**, *82*, 711–732.
- 971 [45] Chodera, J. D.; Shirts, M. R. Replica exchange and expanded ensemble simulations as Gibbs sampling: simple
972 improvements for enhanced mixing. *J. Chem. Phys.* **2011**, *135*, 194110.
- 973 [46] Speidel, J. A.; Banfelder, J. R.; Mezei, M. Automatic control of solvent density in grand canonical ensemble Monte
974 Carlo simulations. *J. Chem. Theory Comput.* **2006**, *2*, 1429–1434.
- 975 [47] Benavides, A. L.; Aragonés, J. L.; Vega, C. Consensus on the solubility of NaCl in water from computer simulations
976 using the chemical potential route. *J. Chem. Phys.* **2016**, *144*, 124504.
- 977 [48] Ross, G. A.; Bodnarchuk, M. S.; Essex, J. W. Water sites, networks, and free energies with grand canonical Monte Carlo.
978 *J. Am. Chem. Soc.* **2015**, *137*, 14930–14943.
- 979 [49] Ross, G. A.; Bruce Macdonald, H. E.; Cave-Ayland, C.; Cabedo Martinez, A. I.; Essex, J. W. Replica exchange and standard
980 state binding free energies with grand canonical Monte Carlo. *J. Chem. Theory Comput.* **2017**,
- 981 [50] Marinari, E.; Parisi, G.; Roma, S.; Vergata, T. Simulated tempering: a new Monte Carlo scheme. **1992**,
- 982 [51] Wang, F.; Landau, D. P. Efficient, multiple-range random walk algorithm to calculate the density of states. *Phys. Rev.*
983 *Lett.* **2001**, *86*, 2050–2053.
- 984 [52] Liang, F. A generalized Wang-Landau algorithm for Monte Carlo computation. *J. Am. Stat. Assoc.* **2005**, *100*, 1311–1327.
- 985 [53] Fukuda, I.; Nakamura, H. Non-Ewald methods: theory and applications to molecular systems. *Biophys. Rev.* **2012**, *4*,
986 161–170.
- 987 [54] Lieb, E. H.; Lebowitz, J. L. The constitution of matter: existence of thermodynamics for systems composed of electrons
988 and nuclei. *Adv. Math.* **1972**, *9*, 316–398.
- 989 [55] Neal, R. M. Annealed Importance Sampling. *arXiv:physics* **1998**, 9803008.
- 990 [56] Karagiannis, G.; Andrieu, C. Annealed importance sampling reversible jump MCMC algorithms. *J. Comput. Graph. Stat.*
991 **2013**, *22*, 623–648.
- 992 [57] Sivak, D. A.; Chodera, J. D.; Crooks, G. E. Using nonequilibrium fluctuation theorems to understand and correct errors
993 in equilibrium and nonequilibrium simulations of discrete Langevin dynamics. *Phys. Rev. X* **2013**, *3*, 011007.
- 994 [58] Wagoner, J. A.; Pande, V. S. Reducing the effect of Metropolization on mixing times in molecular dynamics simulations.
995 *J. Chem. Phys.* **2012**, *137*, 214105.
- 996 [59] Sohl-Dickstein, J. Hamiltonian Monte Carlo with reduced momentum flips. *arXiv:physics* **2012**, 1205.1939.
- 997 [60] Chen, Y.; Roux, B. Efficient hybrid non-equilibrium molecular dynamics - Monte Carlo simulations with symmetric
998 momentum reversal. *J. Chem. Phys.* **2014**, *141*, 114107.

- 999 [61] Elena, A.; Bou-Rabee, N.; Reich, S. A comparison of generalized hybrid Monte Carlo methods with and without
1000 momentum flip. *J. Comput. Phys.* **2009**, *228*, 2256–2265.
- 1001 [62] Leimkuhler, B.; Matthews, C. *Molecular Dynamics: With Deterministic and Stochastic Numerical Methods*; Springer, 2015.
- 1002 [63] OpenMMTools 0.11.1. <https://github.com/choderalab/openmmtools/releases/tag/0.11.1>, 07-06-2017.
- 1003 [64] Amber 14 benchmark archive. http://ambermd.org/Amber14_Benchmark_Suite.tar.bz2, 07-06-2017.
- 1004 [65] Maier, J. A.; Martinez, C.; Kasavajhala, K.; Wickstrom, L.; Hauser, K. E.; Simmerling, C. ff14SB: improving the accuracy
1005 of protein side chain and backbone parameters from ff99SB. *J. Chem. Theory Comput.* **2015**, *11*, 3696–3713.
- 1006 [66] PDBFixer. <https://github.com/pandegroup/pdbfixer>, 07-06-2017.
- 1007 [67] Zgarbová, M.; Šponer, J.; Otyepka, M.; Cheatham, T. E.; Galindo-Murillo, R.; Jurečka, P. Refinement of the sugar-
1008 phosphate backbone torsion beta for AMBER force fields improves the description of Z- and B-DNA. *J. Chem. Theory*
1009 *Comput.* **2015**, *11*, 5723–5736.
- 1010 [68] Joung, I. S.; Cheatham, T. E. Determination of alkali and halide monovalent ion parameters for use in explicitly
1011 solvated biomolecular simulations. *J. Phys. Chem. B* **2008**, *112*, 9020–9041.
- 1012 [69] Barth, E.; Kuczera, K.; Leimkuhler, B.; Skeel, R. D. Algorithms for constrained molecular dynamics. *J. Comput. Chem.*
1013 **1995**, *16*, 1192–1209.
- 1014 [70] Eastman, P.; Pande, V. S. Constant constraint matrix approximation: a robust, parallelizable constraint method for
1015 molecular simulations. *J. Chem. Theory Comput.* **2010**, *6*, 434–437.
- 1016 [71] Miyamoto, S.; Kollman, P. A. Settle: an analytical version of the SHAKE and RATTLE algorithm for rigid water models. *J.*
1017 *Comput. Chem.* **1992**, *13*, 952–962.
- 1018 [72] Chodera, J. D. A simple method for automated equilibration detection in molecular simulations. *J. Chem. Theory*
1019 *Comput.* **2016**, *12*, 1799–1805.
- 1020 [73] van der Walt, S.; Colbert, S. C.; Varoquaux, G. The NumPy array: a structure for efficient numerical computation.
1021 *Comput. Sci. Eng.* **2011**, *13*, 22–30.
- 1022 [74] Jones, E.; Oliphant, T.; Peterson, P. SciPy 0.19.1. <http://www.scipy.org>, 06-23-2017.
- 1023 [75] pymbar 3.0.1. <https://github.com/choderalab/pymbar>, 2-3-2017.
- 1024 [76] McGibbon, R. T.; Beauchamp, K. A.; Harrigan, M. P.; Klein, C.; Swails, J. M.; Hernández, C. X.; Schwantes, C. R.; Wang, L.-
1025 P.; Lane, T. J.; Pande, V. S. MDTraj: a modern open library for the analysis of molecular dynamics trajectories. *Biophys.*
1026 *J.* **2015**, *109*, 1528–1532.
- 1027 [77] Humphrey, W.; Dalke, A.; Schulten, K. VMD: visual molecular dynamics. *J. Mol. Graph.* **1996**, *14*, 33–38.
- 1028 [78] Hunter, J. D. Matplotlib: A 2D graphics environment. *Comput. Sci. Eng.* **2007**, *9*, 90–95.
- 1029 [79] Jorgensen, W. L.; Blake, J. F.; Buckner, Free energy of TIP4P water and the free energies of hydration of CH₄ and Cl-
1030 from statistical perturbation theory. *Chem. Phys.* **1989**, *129*, 193–200.
- 1031 [80] Marcus, Y. Thermodynamics of solvation of ions. Part 5. Gibbs free energy of hydration at 298.15 K. *J. Chem. Soc.,*
1032 *Faraday Trans.* **1991**, *87*, 2995–2999.
- 1033 [81] Noyes, R. M. Thermodynamics of Ion Hydration as a Measure of Effective Dielectric Properties of Water. *J. Am. Chem.*
1034 *Soc.* **1962**, *84*, 513–522.
- 1035 [82] Schmid, R.; Miah, A. M.; Sapunov, V. N. A new table of the thermodynamic quantities of ionic hydration: values and
1036 some applications (enthalpy-entropy compensation and Born radii). *Phys. Chem. Chem. Phys.* **2000**, *2*, 97–102.
- 1037 [83] Sastre de Vicente, M. E. The concept of ionic strength eighty years after its introduction in chemistry. *J. Chem. Educ.*
1038 **2004**, *81*, 750–753.
- 1039 [84] Crooks, G. E. Measuring thermodynamic length. *Phys. Rev. Lett.* **2007**, *99*, 100602.
- 1040 [85] Minh, D. D. L.; Chodera, J. D. Estimating equilibrium ensemble averages using multiple time slices from driven
1041 nonequilibrium processes: Theory and application to free energies, moments, and thermodynamic length in single-
1042 molecule pulling experiments. *J. Chem. Phys.* **2011**, *134*, 024111.

- 1043 [86] Sivak, D. A.; Crooks, G. E. Thermodynamic metrics and optimal paths. *Phys. Rev. Lett.* **2012**, *108*, 190602.
- 1044 [87] Rotskoff, G. M.; Crooks, G. E. Optimal control in nonequilibrium systems: dynamic Riemannian geometry of the Ising
1045 model. *Phys. Rev. E* **2015**, *92*, 060102.
- 1046 [88] Gingrich, T. R.; Rotskoff, G. M.; Crooks, G. E.; Geissler, P. L. Near-optimal protocols in complex nonequilibrium
1047 transformations. *Proc. Natl. Acad. Sci.* **2016**, *113*, 10263–10268.
- 1048 [89] Webb, B. A.; Chimenti, M.; Jacobson, M. P.; Barber, D. L. Dysregulated pH: a perfect storm for cancer progression. *Nat.*
1049 *Rev. Cancer* **2011**, *11*, 671–677.
- 1050 [90] Spahn, V.; Del Vecchio, G.; Labuz, D.; Rodriguez-Gaztelumendi, A.; Massaly, N.; Temp, J.; Durmaz, V.; Sabri, P.; Reidel-
1051 bach, M.; Machelska, H.; et al., A nontoxic pain killer designed by modeling of pathological receptor conformations.
1052 *Science* **2017**, *355*, 966–969.
- 1053 [91] Salvatier, J.; Wiecki, T.; Fonnesbeck, C. Probabilistic programming in Python using PyMC3. *PeerJ Computer Science*
1054 **2016**, *2*, e55.
- 1055 [92] Andrieu, C.; Thoms, J. A tutorial on adaptive MCMC. *Stat. Comput.* **2008**, *18*, 343–373.
- 1056 [93] Haario, H.; Saksman, E.; Tamminen, J. An adaptive Metropolis algorithm. *Bernoulli* **2001**, *7*, 223–242.
- 1057 [94] Atkinson, C.; Mitchell, A. F. Rao's distance measure. *Sankhyā Series A* **1981**, *43*, 345–365.
- 1058 [95] Radak, B. K.; Roux, B. Efficiency in nonequilibrium molecular dynamics Monte Carlo simulations. *J. Chem. Phys.* **2016**,
1059 *145*, 134109.

1060 Appendix 1

1061 Symbols and their definitions

- 1062 • x : Instantaneous configuration (positions, box vectors)
- 1063 • $N_{\text{H}_2\text{O}}$: Number of water molecules
- 1064 • N_{Na^+} : Number of cations
- 1065 • N_{Cl^-} : Number of anions
- 1066 • N_{NaCl} : Number of salt pairs beyond minimal neutralizing ions; equal to $\min\{N_{\text{Na}^+}, N_{\text{Cl}^-}\}$
- 1067 • N : Sum of total number of waters and ions in the system
- 1068 • θ : Vector species labels with N elements that identifies which molecules are waters and which
- 1069 are ions; $\theta_i = 0$ indicates water, $\theta_i = +1$ indicates monovalent cations, and $\theta_i = -1$ indicates
- 1070 monovalent anions
- 1071 • z : total charge number of the macromolecules in the simulation
- 1072 • $n(\theta)$: total charge number of the ions in the simulation
- 1073

$$1074 \quad n(\theta) = \sum_{i=1}^N \theta_i \quad (26)$$

- 1077 • $U(x, \theta)$: Potential energy for a system with configuration x and water/ion identities θ , units of
- 1078 energy
- 1079 • p : External pressure, units of energy \cdot length $^{-3}$
- 1080 • V : Instantaneous box volume, units of length 3
- 1081 • T : Absolute temperature, units of temperature
- 1082 • k_B : Boltzmann constant, units of energy \cdot temperature $^{-1}$
- 1083 • β : Inverse temperature ($\equiv 1/k_B T$), units of energy $^{-1}$
- 1084 • I : Ionic strength, where instantaneous ionic strength for configuration x is given by
- 1085

$$1086 \quad I(x, \theta) \equiv \frac{1}{2} \frac{1}{V(x)} \left(z^2 + \sum_{i=1}^N \theta_i^2 \right) \quad (27)$$

1087 Note that ionic strength includes minimal neutralizing counterions in the sum.

- 1089 • $\Delta\mu$: Chemical potential difference for extracting a NaCl molecule from bulk water and depositing
- 1090 two water molecules to bulk water; an abbreviation of $\Delta\mu_{2\text{H}_2\text{O}-\text{NaCl}}$
- 1091 • $f(N_{\text{NaCl}})$: Free energy to replace $2N_{\text{H}_2\text{O}}$ water molecules with N_{NaCl} salt pairs in bulk water; an
- 1092 abbreviation of $f(N_{\text{NaCl}}, N, p, T)$.
- 1093 • $\Delta f(N_{\text{NaCl}})$: Free energy to add one more salt pair and remove two additional water molecules
- 1094 in a box of water than contains N_{NaCl} salt pairs already; equal to $f(N_{\text{NaCl}} + 1) - f(N_{\text{NaCl}})$; an
- 1095 abbreviation of $\Delta f(N_{\text{NaCl}}, N, p, T)$
- 1096 • $Z(N_{\text{NaCl}}, N, p, T)$: Isothermal-isobaric configurational partition function
- 1097

$$1098 \quad Z(N_{\text{NaCl}}, N, p, T) \equiv \int dx e^{-\beta[U(x; N_{\text{NaCl}}) + pV(x)]} \quad (28)$$

- 1100 • $\Xi(\Delta\mu, N, p, T)$: Semigrand-isothermal-isobaric configurational partition function expressed as a
- 1101 sum over all θ
- 1102

$$1103 \quad \Xi(\Delta\mu, N, p, T) = \sum_{\theta} \delta(n(\theta), -z) \int dx e^{-\beta[U(x, \theta) + pV(x) + \Delta\mu N_{\text{NaCl}}(\theta)]}, \quad (29)$$

1104 and expressed as a sum of number of ions and water molecules

1109

1110

1111

$$\Xi(\Delta\mu, N, p, T) \equiv \sum_{N_{\text{NaCl}}=0}^{N/2} \frac{N!}{N_{\text{Na}^+}!N_{\text{Cl}^-}!N_{\text{H}_2\text{O}}!} Z(N_{\text{NaCl}}, N, p, T) e^{\beta\Delta\mu N_{\text{NaCl}}}, \quad (30)$$

1112

1113

where $N_{\text{NaCl}} = \min\{N_{\text{Na}^+}, N_{\text{Cl}^-}\}$ and $N = N_{\text{Na}^+} + N_{\text{Cl}^-} + N_{\text{H}_2\text{O}}$. The upper bound of the summation—valid when $z = 0$ and N is even—is required as two water molecules are removed for every N_{NaCl} .

1114

1115

1116

1117

- $\pi(x, \theta; N, p, T, \mu)$: Semigrand-isothermal-isobaric probability density with charge neutrality constraint

1119

1120

$$\pi(x, \theta; \Delta\mu, N, p, T) = \frac{1}{\Xi(\Delta\mu, N, p, T)} \delta(n(\theta), -z) e^{-\beta[U(x, \theta) + pV(x) + \Delta\mu N_{\text{NaCl}}(\theta)]}, \quad (31)$$

1121

1122

where the dependence of $\pi(x, \theta; \Delta\mu, N, p, T)$ on z is omitted for brevity

1123

1124

- $\langle A \rangle_{\Delta\mu, N, p, T}$: Expectation of $A(x, \theta)$ in $(\Delta\mu, N, p, T)$ ensemble

1125

1126

$$\langle A \rangle_{\Delta\mu, N, p, T} \equiv \frac{1}{\Xi(\Delta\mu, N, p, T)} \sum_{\theta} \delta(n(\theta), -z) \int dx A(x, \theta) e^{-\beta[U(x, \theta) + pV(x) + \Delta\mu N_{\text{NaCl}}(\theta)]} \quad (32)$$

1127

1128

1129

- $\langle A \rangle_{N_{\text{NaCl}}, N, p, T}$: Expectation of $A(x)$ in $(N_{\text{NaCl}}, N, p, T)$ ensemble

1130

1131

$$\langle A \rangle_{N_{\text{NaCl}}, N, p, T} \equiv \frac{1}{Z(N_{\text{NaCl}}, N, p, T)} \int dx A(x) e^{-\beta[U(x; N_{\text{NaCl}}) + pV(x)]} \quad (33)$$

1132 Appendix 2

1133

Salt concentration in the thermodynamic limit

1134

The purpose of this section is to derive an expression that relates the chemical potential to the salt concentration in a macroscopic saline reservoir (equation 19). This relationship is used in the calibration of our osmostat. The derivation will proceed by first, justifying the macroscopic concentration as the thermodynamic limit of the mean concentration, and second, rewriting the resultant expression in a manner that is amenable to computation.

1135

1136

1137

1138

The mean concentration in the thermodynamic limit

1139

1140

Following the definition of the concentration given in equation 20, the mean salt concentration in the semigrand ensemble considered here is given by

1141

1142

$$\langle c \rangle_{\Delta\mu, N, p, T} = \left\langle \frac{N_{\text{NaCl}}(\theta)}{V(x)} \right\rangle_{\Delta\mu, N, p, T}. \quad (34)$$

1143

1144

1145

1146

1147

We seek an approximation to this expression that it is appropriate for large, macroscopic amounts of liquid saline. For brevity, all expectation values with respect to the thermodynamic ensemble $(\Delta\mu, N, p, T)$ in this section will henceforth be abbreviated as $\langle \cdot \rangle$.

The concentration is a function of two correlated random variables, the number of salt pairs $N_{\text{NaCl}}(\theta)$ and the total volume $V(x)$. A common way to approximate the expectation value, or mean, of a function of random variables is to perform a Taylor expansion about the mean of the arguments. The Taylor expansion (up to the second-order) of the function $g(a, b)$ about the means $\langle a \rangle$ and $\langle b \rangle$, is

$$\begin{aligned} g(a, b) &= g(\langle a \rangle, \langle b \rangle) + \frac{\partial g}{\partial a} \Big|_{\langle a \rangle, \langle b \rangle} (a - \langle a \rangle) + \frac{\partial g}{\partial b} \Big|_{\langle a \rangle, \langle b \rangle} (b - \langle b \rangle) + \frac{1}{2} \frac{\partial^2 g}{\partial a^2} \Big|_{\langle a \rangle, \langle b \rangle} (a - \langle a \rangle)^2 \\ &+ \frac{1}{2} \frac{\partial^2 g}{\partial b^2} \Big|_{\langle a \rangle, \langle b \rangle} (b - \langle b \rangle)^2 + \frac{\partial^2 g}{\partial a \partial b} \Big|_{\langle a \rangle, \langle b \rangle} (a - \langle a \rangle)(b - \langle b \rangle) + \dots \end{aligned} \quad (35)$$

This expansion is particularly useful because the first order terms of the expanded mean $\langle g(a, b) \rangle$ are zero i.e. $\langle a - \langle a \rangle \rangle = 0$ and $\langle b - \langle b \rangle \rangle = 0$. Hence, truncating the expansion to the second order leaves us with the approximation

$$\begin{aligned} \langle g(a, b) \rangle &\approx g(\langle a \rangle, \langle b \rangle) + \frac{1}{2} \frac{\partial^2 g}{\partial a^2} \Big|_{\langle a \rangle, \langle b \rangle} \langle (a - \langle a \rangle)^2 \rangle + \frac{1}{2} \frac{\partial^2 g}{\partial b^2} \Big|_{\langle a \rangle, \langle b \rangle} \langle (b - \langle b \rangle)^2 \rangle \\ &+ \frac{\partial^2 g}{\partial a \partial b} \Big|_{\langle a \rangle, \langle b \rangle} \langle (a - \langle a \rangle)(b - \langle b \rangle) \rangle \\ &= g(\langle a \rangle, \langle b \rangle) + \frac{1}{2} \frac{\partial^2 g}{\partial a^2} \Big|_{\langle a \rangle, \langle b \rangle} \text{Var}(a) + \frac{1}{2} \frac{\partial^2 g}{\partial b^2} \Big|_{\langle a \rangle, \langle b \rangle} \text{Var}(b) + \frac{\partial^2 g}{\partial a \partial b} \Big|_{\langle a \rangle, \langle b \rangle} \text{Cov}(a, b), \end{aligned} \quad (36)$$

where $\text{Var}(a)$ and $\text{Cov}(a, b)$ denote the variance and covariance, respectively. Returning to the salt concentration, we relate c to the above with $g(N_{\text{NaCl}}, V) = N_{\text{NaCl}}/V$, and evaluate the partial derivatives to find that

$$\langle c \rangle \approx \frac{\langle N_{\text{NaCl}} \rangle}{\langle V \rangle} + \frac{\langle N_{\text{NaCl}} \rangle}{\langle V \rangle^3} \text{Var}(V) - \frac{1}{\langle V \rangle^2} \text{Cov}(V, N_{\text{NaCl}}). \quad (37)$$

The leading term $\langle N_{\text{NaCl}} \rangle / \langle V \rangle$ is the macroscopic expression that we seek. Thus, we require that the variance and covariance terms vanish in the thermodynamic limit. To show that they indeed do, we exploit the useful correspondence between partial derivatives and covariance in statistical thermodynamics. First, note that

$$\begin{aligned} \text{Var}(V) &= (k_B T)^2 \frac{\partial^2 \ln(\Xi)}{\partial p^2} \\ &= -k_B T \frac{\partial \langle V \rangle}{\partial p}, \end{aligned} \quad (38)$$

where $\Xi \equiv \Xi(\Delta\mu, N, p, T)$ and is defined in equation 7. Also, note that

$$\begin{aligned} \text{Cov}(V, N_{\text{NaCl}}) &= (k_B T)^2 \frac{\partial^2 \ln(\Xi)}{\partial p \partial \Delta\mu} \\ &= k_B T \frac{\partial \langle V \rangle}{\partial \Delta\mu}. \end{aligned} \quad (39)$$

Second, we make use of the isothermal compressibility

$$\kappa_T \equiv -\frac{1}{\langle V \rangle} \frac{\partial \langle V \rangle}{\partial p}, \quad (40)$$

and introduce the isothermal susceptibility of the volume with respect to the chemical potential

$$\chi_T \equiv \frac{1}{\langle V \rangle} \frac{\partial \langle V \rangle}{\partial \Delta\mu}, \quad (41)$$

The susceptibilities κ_T and χ_T are bulk properties that measure the relative amount the volume of a system responds to changes in pressure and chemical potential, respectively. They are intensive quantities, such that they do not scale with the size of the system. These allow us to re-write the approximation of the mean concentration (equation 37) as

$$\langle c \rangle \approx \frac{\langle N_{\text{NaCl}} \rangle}{\langle V \rangle} - \frac{1}{k_B T} \frac{\langle N_{\text{NaCl}} \rangle}{\langle V \rangle^2} \kappa_p - \frac{1}{k_B T} \frac{1}{\langle V \rangle} \chi_T. \quad (42)$$

To proceed, note that in the second term, both N_{NaCl} and $\langle V \rangle$ are extensive, and rise in proportion to the total number of molecules in the system N . Thus, approximating the mean concentration as $\langle N_{\text{NaCl}} \rangle / \langle V \rangle$ incurs an error that is $\mathcal{O}(\langle V \rangle^{-1})$, which tends to zero in the thermodynamic limit. We therefore define the macroscopic concentration of a saline reservoir as

$$\langle \hat{c} \rangle \equiv \frac{\langle N_{\text{NaCl}} \rangle}{\langle V \rangle}. \quad (43)$$

We require the macroscopic concentration to be amenable to computational analysis

While the expression for the macroscopic concentration above does not appear immediately useful, we now show how $\langle \hat{c} \rangle$ can be calculated for wide range of applied chemical potentials by pre-calculating the free energies to insert salt into a system, $f(N_{\text{NaCl}}) (\equiv f(N_{\text{NaCl}}, \Delta\mu, N, p, T))$, and the average volume as a function of the number of salt pairs, $\langle V \rangle_{N_{\text{NaCl}}} (\equiv \langle V \rangle_{N_{\text{NaCl}}, N, p, T})$.

To begin, it is useful to expand the definition of $\langle N_{\text{NaCl}} \rangle$ given by equation 17 into

$$\langle N_{\text{NaCl}} \rangle = \frac{\sum_{N_{\text{NaCl}}=0} N_{\text{NaCl}} e^{-f(N_{\text{NaCl}}) + \beta \Delta\mu N_{\text{NaCl}}}}{\sum_{N_{\text{NaCl}}=0} e^{-f(N_{\text{NaCl}}) + \beta \Delta\mu N_{\text{NaCl}}}}. \quad (44)$$

Next, we derive an expression for $\langle V \rangle$ that will cancel with the denominator of equation 44 when evaluating $\langle \hat{c} \rangle$. Using the representation of the semigrand density given by equation 8, the mean

volume is given by

$$\begin{aligned}
 \langle V \rangle &= \frac{\sum_{N_{\text{NaCl}}=0} \int dx V(x) e^{-\beta(U(x; N_{\text{NaCl}}) + pV(x) + \Delta\mu N_{\text{NaCl}}(\theta))}}{\sum_{N_{\text{NaCl}}=0} e^{-f(N_{\text{NaCl}}) + \beta\Delta\mu N_{\text{NaCl}}}} \\
 &= \frac{\sum_{N_{\text{NaCl}}=0} e^{\beta\Delta\mu N_{\text{NaCl}}} \int dx V(x) e^{-\beta(U(x; N_{\text{NaCl}}) + pV(x))}}{\sum_{N_{\text{NaCl}}=0} e^{-f(N_{\text{NaCl}}) + \beta\Delta\mu N_{\text{NaCl}}}} \\
 &= \frac{\sum_{N_{\text{NaCl}}=0} e^{\beta\Delta\mu N_{\text{NaCl}}} \int dx V(x) e^{-\beta(U(x; N_{\text{NaCl}}) + pV(x))} \cdot \int dx' e^{-\beta(U(x'; N_{\text{NaCl}}) + pV(x'))}}{\sum_{N_{\text{NaCl}}=0} e^{-f(N_{\text{NaCl}}) + \beta\Delta\mu N_{\text{NaCl}}} \cdot \int dx'' e^{-\beta(U(x''; N_{\text{NaCl}}) + pV(x''))}} \\
 &= \frac{\sum_{N_{\text{NaCl}}=0} e^{\beta\Delta\mu N_{\text{NaCl}}} \langle V \rangle_{N_{\text{NaCl}}} \cdot e^{-f(N_{\text{NaCl}})}}{\sum_{N_{\text{NaCl}}=0} e^{-f(N_{\text{NaCl}}) + \beta\Delta\mu N_{\text{NaCl}}}} \\
 &= \frac{\sum_{N_{\text{NaCl}}=0} \langle V \rangle_{N_{\text{NaCl}}} e^{-f(N_{\text{NaCl}}) + \beta\Delta\mu N_{\text{NaCl}}}}{\sum_{N_{\text{NaCl}}=0} e^{-f(N_{\text{NaCl}}) + \beta\Delta\mu N_{\text{NaCl}}}}, \tag{45}
 \end{aligned}$$

where the third and fourth line exploit the definition of the ensemble average for a fixed N_{NaCl} . Inserting the expressions for the average number of salt pairs (equation 44) and the average volume (equation 45) into the macroscopic concentration (equation 43), we arrive at

$$\langle \hat{c} \rangle = \frac{\sum_{N_{\text{NaCl}}=0} N_{\text{NaCl}} e^{-f(N_{\text{NaCl}}) + \beta\Delta\mu N_{\text{NaCl}}}}{\sum_{N_{\text{NaCl}}=0} \langle V \rangle_{N_{\text{NaCl}}} e^{-f(N_{\text{NaCl}}) + \beta\Delta\mu N_{\text{NaCl}}}},$$

which is the same as equation 19 from the main text. Pertinently, the denominators in equations 44 and 45 have canceled, which greatly simplifies the evaluation of the macroscopic concentration for a given $\Delta\mu$.

The magnitude of salt fluctuations

The concentration of salt fluctuates in osmostat simulations. This section briefly outlines how one would expect the magnitude of salt fluctuations to vary with the size of the system based on statistical mechanical principles. By differentiating equation 17, one can show that the variance of the number of salt pairs N_{NaCl} is proportional to the gradient of $\langle N_{\text{NaCl}} \rangle$ with respect to the chemical potential $\Delta\mu$, specifically

$$\text{Var}(N_{\text{NaCl}}) = k_B T \frac{\partial \langle N_{\text{NaCl}} \rangle}{\partial \Delta\mu}. \tag{46}$$

By dividing both sides by $\langle N_{\text{NaCl}} \rangle$, i.e.

$$\frac{1}{\langle N_{\text{NaCl}} \rangle} \text{Var}(N_{\text{NaCl}}) = \frac{1}{\langle N_{\text{NaCl}} \rangle} k_B T \frac{\partial \langle N_{\text{NaCl}} \rangle}{\partial \Delta\mu}, \tag{47}$$

reveals that $\frac{1}{\langle N_{\text{NaCl}} \rangle} \text{Var}(N_{\text{NaCl}})$ is proportional to the *relative* change in the mean of N_{NaCl} in response to altering the chemical potential. As the right-hand-side of the above equation is an intensive quantity, $\frac{1}{\langle N_{\text{NaCl}} \rangle} \text{Var}(N_{\text{NaCl}})$ is also an intensive, implying that

$$\text{Var}(N_{\text{NaCl}}) \propto N_{\text{NaCl}}. \tag{48}$$

Therefore, the scale of the fluctuations in salt amount, as measured by the standard deviation, grows as $\langle N_{\text{NaCl}} \rangle^{1/2}$.

In contrast to the amount of salt, the size of the fluctuations of salt concentration *decreases* with the size of aqueous systems. Water is a highly incompressible fluid, such that small changes in pressure have a very small effect on the volume of aqueous systems. From equations 38 and 40, a low isothermal compressibility implies that the variance of the volume is small with respect to the mean volume (i.e. the relative variance). Assuming that the relative variance of the volume is smaller

1246

1247

1248

1249

1250

1251

1252

1253

1254

1255

1256

1257

than the relative variance of the number of salt pairs, one can use the same approach as that of equation 35 to show that

$$\text{Var}(c) = \text{Var}\left(\frac{N_{\text{NaCl}}}{V}\right) \quad (49)$$

$$\approx \frac{1}{\langle V \rangle^2} \text{Var}(N_{\text{NaCl}}) \quad (50)$$

Using the fact that, for bulk-like water, $\langle V \rangle \propto \langle N_{\text{H}_2\text{O}} \rangle \propto \langle N_{\text{NaCl}} \rangle$ along with equation 48, we arrive at $\text{Var}(c) \sim \langle N_{\text{NaCl}} \rangle^{-1}$ for systems with large amounts of water. Thus, the standard deviation of the salt concentration scales like $\langle N_{\text{H}_2\text{O}} \rangle^{-1/2}$ or $\langle N_{\text{NaCl}} \rangle^{-1/2}$ for a fixed chemical potential.

1258 Appendix 3

1259 Algorithmic implementation of the osmostat

1260 This section describes the Metropolis-Hastings procedure from Saltswap [0.52] used to insert and
 1261 delete salt. Insertion and deletion moves were enhanced with NCMC³². To describe its implemen-
 1262 tation of NCMC within SaltSwap, a more compressed notation is used compared to the original
 1263 publication. For a more general and detailed exposition on NCMC, we refer readers to the original
 1264 manuscript.

1265 The osmostat move begins with the random choice of whether to insert or delete salt. The protocol
 1266 is denoted $\Lambda \in \{ \Lambda_{\text{insert}}, \Lambda_{\text{delete}} \}$, and the time reversed protocol is denoted $\bar{\Lambda}$, where $\bar{\Lambda}_{\text{insert}} = \Lambda_{\text{delete}}$
 1267 and $\bar{\Lambda}_{\text{delete}} = \Lambda_{\text{insert}}$. The probability to insert or delete a salt pair, $P(\Lambda | N_{\text{NaCl}})$, depends on the number
 1268 of salt molecules, N_{NaCl} , in the system in the following way:

$$1270 P(\Lambda_{\text{insert}} | N_{\text{NaCl}}) = \begin{cases} 1 & \text{if } N_{\text{NaCl}} = 0; \\ 1/2 & \text{if } 0 < N_{\text{NaCl}} < N_{\text{NaCl,max}}; \\ 0 & \text{if } N_{\text{NaCl}} = N_{\text{NaCl,max}}; \end{cases} \quad (51)$$

$$1273 P(\Lambda_{\text{delete}} | N_{\text{NaCl}}) = \begin{cases} 0 & \text{if } N_{\text{NaCl}} = 0; \\ 1/2 & \text{if } 0 < N_{\text{NaCl}} < N_{\text{NaCl,max}}; \\ 1 & \text{if } N_{\text{NaCl}} = N_{\text{NaCl,max}}; \end{cases} \quad (52)$$

1277 where for all simulations except the SAMS calibration simulations, $N_{\text{NaCl,max}} = \frac{1}{2}(N - (N \bmod 2))$ was
 1278 chosen as two water molecules are required for the insertion of a Na^+ and Cl^- pair. In the SAMS
 1279 calibration simulations, $N_{\text{NaCl,max}}$ was set to twenty. The particular choices of $P(\Lambda_{\text{delete}} | N_{\text{NaCl}})$ and
 1280 $P(\Lambda_{\text{insert}} | N_{\text{NaCl}})$ ensure that insertions are always attempted when there is no salt in the system, and
 1282 deletions are always attempted when the number of salt pairs has reached maximum capacity.

1283 For the insertion of salt, any two water molecules could be selected for transformation into Na^+
 1284 and Cl^- . Similarly, for the removal of salt, any Na^+ ion and Cl^- ion could be selected for transformation
 1285 into two water molecules. Formally, let $S(N)$ denote the set $\{1, 2, \dots, N\}$, i.e. the set of indices for all
 1286 water molecules and ions. For salt insertion, the index of candidate Na^+ ion was a random uniform
 1287 sample from the set $\{i \in S(N) : \theta_i = 0\}$ and the index of the Cl^- ion was a random uniform sample
 1288 from the set $\{j \in S(N) : \theta_j = 0, i \neq j\}$. For salt removal, indices were selected randomly and
 1289 uniformly from the sets $\{i \in S(N) : \theta_i = +1\}$ and $\{j \in S(N) : \theta_j = -1\}$. As indices were chosen
 1290 with equal probability within each set of possible candidates, the ratio of selection probabilities for
 1291 molecule indices for forward and reverse protocols are given by

$$1292 \frac{P(i, j | \Lambda_{\text{insert}})}{P(i, j | \Lambda_{\text{delete}})} = \frac{N_{\text{H}_2\text{O}}(N_{\text{H}_2\text{O}} - 1)}{(N_{\text{Na}^+} + 1)(N_{\text{Cl}^-} + 1)}, \quad (53)$$

1294 and

$$1296 \frac{P(i, j | \Lambda_{\text{delete}})}{P(i, j | \Lambda_{\text{insert}})} = \frac{N_{\text{Na}^+} N_{\text{Cl}^-}}{(N_{\text{H}_2\text{O}} + 1)(N_{\text{H}_2\text{O}} + 2)} \quad (54)$$

1298 Following the choice of protocol and pair of molecules that would be transmuted, NCMC was
 1299 used to enhance the efficiency of the insertion or deletion attempt. This implementation of NCMC
 1300 consists of a fixed series of *perturbation* and *propagation* kernels over a fixed alchemical path. For
 1301 both insertion and deletion moves, the alchemical path is a linear interpolation the nonbonded
 1302 parameters of the water model and the ions. This particular alchemical path ensured that charge
 1303 neutrality was maintained throughout the NCMC procedure.

1304
1305
1306
1307
1308
1309
1310
1311
1312
1313
1314
1315
1316
1317
1318
1319
1320
1321
1322
1323
1324
1325
1326
1327

1328
1329
1330
1331
1332
1333
1334
1335
1336
1337
1338
1339
1340
1341
1342
1343
1344
1345
1346
1347
1348
1349
1350
1351

The alchemical path is broken up into T segments that are uniformly spaced with respect to the nonbonded parameters. At state t , the configuration of the system will be denoted as x_t and the values of the nonbonded parameters for molecules i and j will be denoted as λ_t^{ij} . A single NCMC *step* corresponds to the application of the perturbation kernel followed by a the propagation kernel. When in state t , the perturbation kernel updates the nonbonded parameters $(x_t, \lambda_t^{ij}) \rightarrow (x_t, \lambda_{t+1}^{ij})$, and the propagation kernel updates the configuration $(x_t, \lambda_{t+1}^{ij}) \rightarrow (x_{t+1}, \lambda_{t+1}^{ij})$. Each propagation kernel consists of K steps of Langevin dynamics using the parameters described in Simulation Details. A propagation kernel is also applied to the system before the first perturbation kernel to ensure the time symmetry of the protocol. The instantaneous change in the potential energy that results from the application of the perturbation kernel is recorded for each NCMC step and summed to produce the total work performed on the system by the protocol:

$$W^{ij}(X_T, \Lambda) = \sum_{t=1}^T U(x_t, \lambda_{t+1}^{ij}) - U(x_t, \lambda_t^{ij}), \quad (55)$$

where the nonequilibrium trajectory $X_T \equiv (x_0, x_1, \dots, x_T)$. The difference between the protocol work and applied chemical potential $\Delta\mu$, along with the move proposal probabilities, determines whether a move is accepted or rejected. For the insertion of salt $\Delta\mu(\Lambda_{\text{insert}}) = 2\mu_{\text{H}_2\text{O}} - \mu_{\text{NaCl}}$, and for the deletion of salt $\Delta\mu(\Lambda_{\text{delete}}) = 2\mu_{\text{NaCl}} - \mu_{\text{H}_2\text{O}}$. Attempts are accepted with the following probability

$$A^{ij}(X_T, \Lambda) = \min \left\{ 1, \frac{P(i, j | \tilde{\Lambda}) P(\tilde{\Lambda} | \tilde{N}_{\text{NaCl}})}{P(i, j | \Lambda) P(\Lambda | N_{\text{NaCl}})} \exp(-\beta W^{ij}(X_T, \Lambda) + \beta \Delta\mu(\Lambda)) \right\}. \quad (56)$$

To preserve pathwise detailed balance, velocities were reversed upon acceptance. If a move is accepted, θ_i and θ_j are updated to reflect the new molecule identities.

Pseudo-code for the NCMC osmostat with molecular dynamics

This section contains the pseudo-code of the production osmostat simulations.

Begin algorithm

Choose a macroscopic salt concentration \hat{c} .
 Infer the chemical potential $\Delta\mu$ by inverting equation 19.
 Initialize position and velocity (x_0, v_0) , state vector θ_0 , and maximum number of iterations M .
for $i \in \{1, 2, \dots, M\}$ **do**
 Sample conformations
 Perform 4 ps of Langevin integration with a fixed amount of salt:
 $(x_i^*, v_i^*) \leftarrow \text{Integrate}((x_{i-1}, v_{i-1}), 4 \text{ ps})$.
 Sample salt concentration
 Randomly select whether to add or remove salt as well as which molecules will be transmuted.
 Define the trial state vector as θ^* .
 Define initial and final nonbonded parameters: $(q_{\text{initial}}, \sigma_{\text{initial}}, \epsilon_{\text{initial}})$ and $(q_{\text{final}}, \sigma_{\text{final}}, \epsilon_{\text{final}})$.
 procedure NCMC($(q_{\text{initial}}, \sigma_{\text{initial}}, \epsilon_{\text{initial}}), (q_{\text{final}}, \sigma_{\text{final}}, \epsilon_{\text{final}}), (x_i^*, v_i^*), \theta^*$)
 Initialize variables, including protocol work W :
 $W^0 \leftarrow 0$
 $(q^0, \sigma^0, \epsilon^0) \leftarrow (q_{\text{initial}}, \sigma_{\text{initial}}, \epsilon_{\text{initial}})$
 $(x_i^0, v_i^0) \leftarrow \text{Integrate}((x_i^*, v_i^*), 20 \text{ fs})$
 for $k \in \{1, 2, \dots, 1000\}$ **do**
 Linear interpolation of the nonbonded parameters:
 $f^k = k/1000$
 for all atoms in the molecule **do**

```
1352      $q^k \leftarrow (1 - f^k)q_{\text{initial}} + f^k q_{\text{final}}$ 
1353      $\sigma^k \leftarrow (1 - f^k)\sigma_{\text{initial}} + f^k \sigma_{\text{final}}$ 
1354      $\epsilon^k \leftarrow (1 - f^k)\epsilon_{\text{initial}} + f^k \epsilon_{\text{final}}$ 
1355     end for
1356     Update the protocol work:
1357      $W^k \leftarrow W^{k-1} + U(x_i^{k-1}; q^k, \sigma^k, \epsilon^k) - U(x_i^{k-1}; q^{k-1}, \sigma^{k-1}, \epsilon^{k-1})$ 
1358     Propagate the system:
1359      $(x_i^k, v_i^k) \leftarrow \text{Integrate}((x_i^{k-1}, v_i^{k-1}), 20 \text{ fs})$ 
1360     end for
1361     Accept or reject using acceptance criterion  $A(W^k, \Delta\mu, \theta^*)$ 
1362     if Accept move then
1363         Keep final positions and state vector but reverse velocities:
1364          $(x_i, v_i) \leftarrow (x_i^k, -v_i^k)$ 
1365          $\theta_i \leftarrow \theta^*$ 
1366     else
1367         Return positions, velocities and the state vector to after equilibrium sampling:
1368          $(x_i, v_i) \leftarrow (x_i^*, v_i^*)$ 
1369          $\theta_i \leftarrow \theta_{i-1}$ 
1370     end if
1371     end procedure
1372 end for
1373 End algorithm
```

1374 Appendix 4

1375 **Validation: Ideal Mixing with the osmostat**

1376 In the Results section, Figure 4 *top left* indicates that the chemical potential has been properly
 1377 calibrated, and Figure 6 shows that the osmostat produces samples that are concordant with physical-
 1378 chemical intuition. In this section, we apply our osmostat to sample ideal mixing to provide further
 1379 validation of the SaltSwap code base. Ideal mixing can be simulated with our osmostat by ensuring
 1380 that salt insertion and deletion accrue no protocol work. This is implemented by using the same
 1381 forcefield parameters for Na⁺ and Cl⁻ as the water model. As our osmostat also gives the ions the
 1382 same mass as water, the "ions" sampled over in this section are identical to water except for their
 1383 labeling.

1384 To validate the sampling of the osmostat, we require an analytical relationship between the
 1385 chemical potential $\Delta\mu$ and the numbers of salt N_{NaCl} and water molecules $N_{\text{H}_2\text{O}}$. The chemical
 1386 potential used in our osmostat is the difference between the chemical potential of water multiplied
 1387 by two and Na⁺ and Cl⁻:

$$1388 \Delta\mu = 2\mu_{\text{H}_2\text{O}} - \mu_{\text{Na}^+} - \mu_{\text{Cl}^-}. \quad (57)$$

1390 In order to relate $\Delta\mu$ to N_{NaCl} and $N_{\text{H}_2\text{O}}$, we will first consider a solution of water and ions in the
 1391 (N, p, T) ensemble with fixed particle identities, and then relate the result to the $(\Delta\mu, N, p, T)$ ensemble.
 1392 For this fixed identity solution, let $N = N_{\text{H}_2\text{O}} + N_{\text{Na}^+} + N_{\text{Cl}^-}$ and $N_{\text{Na}^+} = N_{\text{Cl}^-}$. In the (N, p, T) ensemble,
 1393 the chemical potential for a species s can be expressed as

$$1394 \mu(N, p, T) = \mu_s^o - kT \ln(x_s \gamma_s(N, p, T)), \quad (58)$$

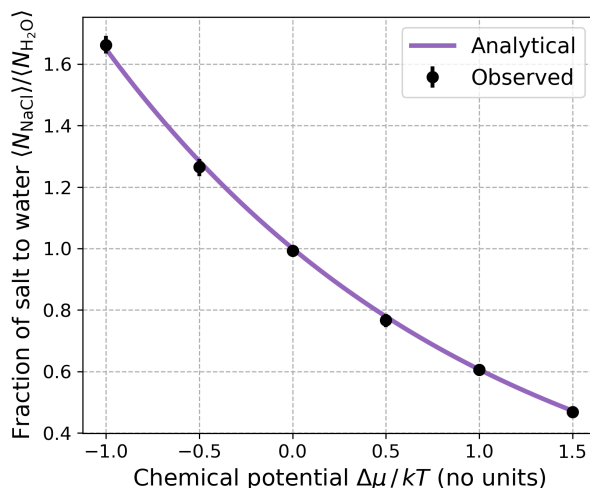
1396 where μ_s^o is the chemical potential of s in some reference state, x_s is the mole fraction of s , and
 1397 $\gamma_s(N, p, T)$ is the activity coefficient of s . In general, the chemical potential is also dependent on the
 1398 composition of the system. When Na⁺ and Cl⁻ have the same forcefield parameters and mass as
 1399 water (i.e they are physically identical), the reference state and activity coefficients must be the same.
 1400 So using equation 58 and 57 we have

$$1402 \begin{aligned} \Delta\mu(N, p, T) &= 2kT \ln(x_{\text{H}_2\text{O}}) - kT \ln(x_{\text{Na}^+}) - kT \ln(x_{\text{Cl}^-}). \\ &= 2kT \ln(x_{\text{H}_2\text{O}}) - 2kT \ln(x_{\text{NaCl}}) \\ &= 2kT \ln\left(\frac{N_{\text{H}_2\text{O}}}{N_{\text{NaCl}}}\right) \end{aligned} \quad (59)$$

1406 where the second line follows from the fact that there are equal numbers of Na⁺ and Cl⁻ ions. In the
 1407 semigrand canonical $(\Delta\mu, N, p, T)$ ensemble that is sampled by our osmostat, the chemical potential
 1408 $\Delta\mu$ is a controlled by the user. As this conjugate to the number of salt pairs, equation 59 will apply to
 1409 the averages $\langle N_{\text{NaCl}} \rangle_{\Delta\mu, N, p, T}$ and $\langle N_{\text{H}_2\text{O}} \rangle_{\Delta\mu, N, p, T}$, so that we have

$$1411 \frac{\langle N_{\text{NaCl}} \rangle_{\Delta\mu, N, p, T}}{\langle N_{\text{H}_2\text{O}} \rangle_{\Delta\mu, N, p, T}} = e^{-\frac{1}{2}\beta\Delta\mu}. \quad (60)$$

1413 To test whether our osmostat correctly samples the average salt to water ratio given in equation 60,
 1414 ideal mixing simulations were performed using SaltSwap on a small box of TIP3P water containing five
 1415 hundred molecules for a range of chemical potentials. Ten thousand insertion and deletion attempts
 1416 were made for salt pairs that had the same forcefield parameters as water. Only one perturbation
 1417 step was used for the ideal NCMC insertion and deletion and the configuration of the system was
 1418 not propagated during attempts. Figure 1 shows that there is excellent agreement between the
 1419 relationship predicted by equation 60 and the simulation data.



1420

1421

1422

1423

1424

1425

1426

1427

1428

1429

1430

Appendix 4 Figure 1. Validating the osmostat by comparing the observed average salt-water fractions to analytical values for ideal mixing.

The relationship between the chemical potential and fraction of average number of salt pairs to water molecules is known exactly for ideal mixing, and is given by equation 60. Ideal mixing was implemented for the osmostat by giving the ions the same forcefield parameters as water. For each simulation at a chemical potential, the equilibration time and statistical inefficiency for the average number of salt pairs $\langle N_{\text{NaCl}} \rangle_{\Delta\mu, N, p, T}$ and water molecules $\langle N_{\text{H}_2\text{O}} \rangle_{\Delta\mu, N, p, T}$ was determined using the timeseries module of pymbar⁷⁵. The automatically determined equilibration times ranged from 361 and 723 insertion or deletion attempts. Effectively independent samples were extracted using the statistical inefficiency, and the means and 95% confidence intervals were estimated using bootstrap analysis.

1431

1432

1433

1434

1435

1436

1437

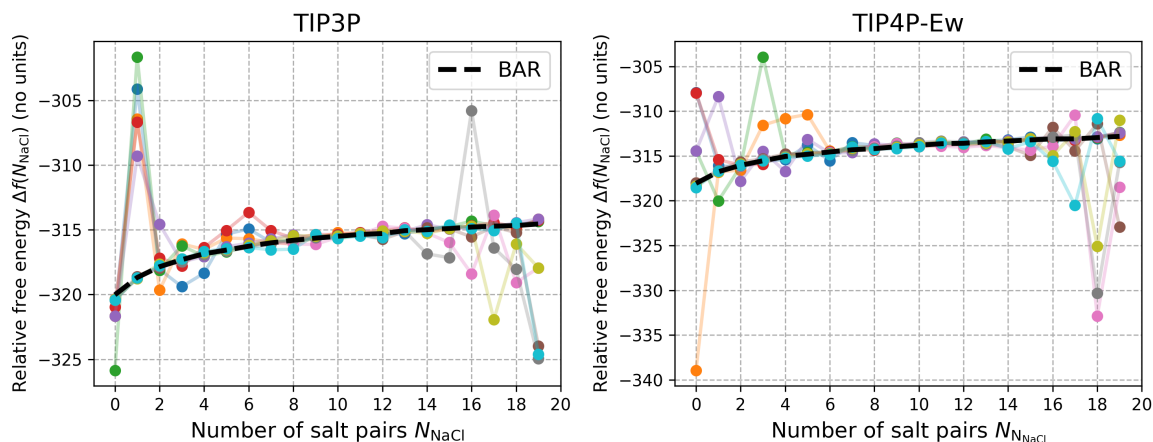
1438

It was also verified that the protocol work was effectively zero for the ideal NCMC transformations. While the protocol work should be exactly zero, the numerical imprecision of our implementation meant this could not always be achieved. The average protocol work for the transformations shown in Figure 1 (which were performed on a CPU Intel Core i7 with one perturbation step) was 1×10^{-7} kT with a maximum absolute value of 8×10^{-5} kT. The NCMC protocol used throughout this study has one thousand perturbation steps and ten propagation steps per perturbation. With this protocol, the average protocol work was estimated using one thousand attempts on a GTX1080 GPU to be 2×10^{-8} kT with a maximum absolute value of 5×10^{-4} kT.

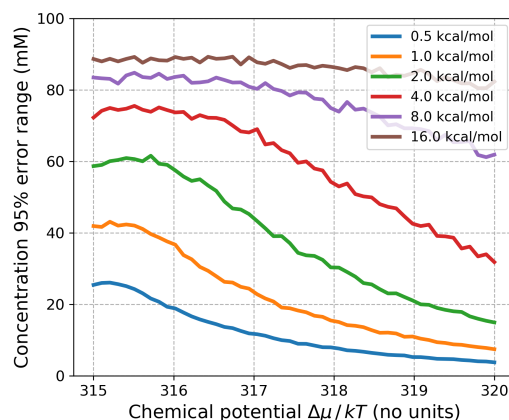
1439 **Appendix 5**

1440

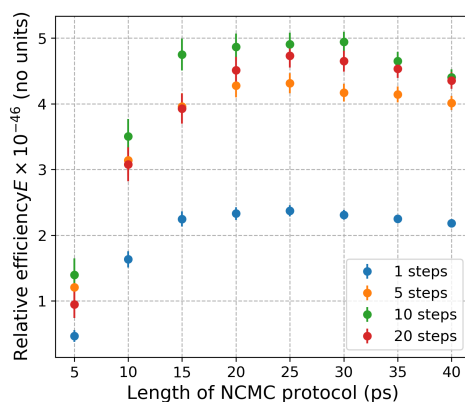
Supplementary figures



Appendix 5 Figure 1. A Comparison of the salt insertion free energies as estimated by SAMS and BAR. The individual SAMS estimates from ten repeats of the relative free energy $\Delta f(N_{NaCl})$ to insert a Na^+ and Cl^- and remove two water molecules in boxes of TIP3P (left) and TIP4P-Ew (right) for each SAMS simulations. Each color represents an estimate of $\Delta f(N_{NaCl})$ from each repeat. The relative free energy as calculated by BAR using all the SAMS simulation data is shown for reference (dotted black line). Five of the SAMS repeats were started with the maximum of 20 salt pairs in the system, and the other five started with none. The significant variation between the individual SAMS repeats is due to the rapid accumulation of the biasing potential in the initial stages of the algorithm. This biased the sampling away from the initial states of the simulations and prevented the uniform sampling over the salt numbers.



Appendix 5 Figure 2. The statistical uncertainty of the predicted macroscopic concentration as a function of the chemical potential for different standard errors of the free energies $f(N_{\text{NaCl}})$ in a box of 887 TIP3P water molecules. Using the data from the SAMS calibration simulations, Gaussian noise, with a mean of zero, was added to each estimated free energy $f(N_{\text{NaCl}})$ $N \in \{0, 1, \dots, 20\}$, for a fixed values of $\langle V \rangle_{N_{\text{NaCl}}}$. Three thousand noisy sample of $f(N_{\text{NaCl}})$ $N \in \{0, 1, \dots, 20\}$, equation 19 were used to predict the macroscopic concentration for a range of chemical potentials. This figure shows the 95% confidence range of the resultant ensemble of concentrations for different standard deviations of the Gaussian noise about the free energies. One needs to evaluate the free energies $f(N_{\text{NaCl}})$ to within 4 kcal/mol to achieve an error in the concentration that is no larger than roughly 80 mM. The tapering of the statistical error in the concentration at lower values of the chemical potential is due to maximum number of salt pairs used in the calibration (20), which limits that maximum concentration that can be predicted.



Appendix 5 Figure 3. The relative efficiency of salt insertions/deletions in TIP3P water for different numbers of NCMC propagation steps between each perturbation step. Due to the manner in which the nonbonded parameters are updated in the SaltSwap code, it is faster—for a fixed protocol time-length—to perform multiple propagation steps for each perturbation (i.e. update of the nonbonded parameters) during an NCMC insertion/deletion attempt. More propagation steps limit the amount of communication between the CPU and GPU. However, for a fixed total protocol time-length, fewer perturbations increases the thermodynamic length each perturbation must traverse, which decreases the mean acceptance rate of the attempts. Thus, there is a (code-dependent) trade-off in the sampling efficiency between the number of perturbations and propagations steps. This figure shows the efficiency, defined by equation 25, for different numbers of propagation steps at different protocol time-lengths relative to the efficiency of instantaneous insertions and deletions. Ten propagation steps per perturbation step achieve the highest efficiencies, and so were used in all production osmostat simulations.